RICE UNIVERSITY LIBRARY
HOUSTON, TEXAS

RICE UNIVERSITY

MAGNETIC PERTURBATIONS DUE TO CURRENT STRUCTURAL VARIATIONS

by

Yuan-Cheng Teng

A THESIS SUBMITTED

IN PARTIAL FULFILLMENT OF THE

REQUIREMENTS FOR THE DEGREE OF

Master of Science

Thesis Director's signature:

Paul A Clinton

Houston, Texas

August 1973

MAGNETIC PERTURBATIONS DUE TO CURRENT STRUCTURAL VARIATIONS

by

Yuan-Cheng Teng

ABSTRACT

Study of the magnetic perturbations caused by auroral currents has been conducted by rocket-borne magnetometer measurements for years. Since the horizontal auroral currents were usually found to be confined near the visible auroral arcs, as determined by Heppner [1954], Davis [1961], and Davis and Kimball [1962], a number of current models have been established in order to explain observed data by rockets or satellite measurements. In those models, the requirement that the current be continuous across the highly conducting arc results in either polarization electric fields to reduce the current in the highly conducting region or Birkeland currents to provide return current to the outer part of the magnetosphere. Boström found two basic solutions, one in which a horizontal electrojet connects two filamentary Birkeland currents, and the other in which broad Birkeland sheet currents (Fig. 2) flow to the edges of the arc, with a transverse closing current and a Hall electrojet. In this thesis, we adopted a model similar to the second solution and

assumed that the arc was bombarded by energetic precipitating electrons.

In this thesis, the effect of a spatial fold on the magnetic vector field in the vicinity of the arc is examined. Fig. 1 shows the current model used in the initial calculations. It has a displacement of thickness of 30 km from its center and is composed of two current parts. One part is the two oppositely directed Birkeland sheet currents having an equal current density of 0.5 amp/m and an equal thickness of 30 km for each sheet, in which the downward current sheet is on the south side of the arc and the upward on the north. And the other part is an electrojet having a magnitude of 5×10^3 amp flowing eastward at an altitude of 100 km. Model computations were performed with the Rice IBM 370/155 computer. The variations of the vector components as well as the directions of the magnetic fields due to the following three cases, such as the electrojet, the sheet currents and the combination of the two along a path of rocket flight were individually included in details. For the electrojet current which was a kinked line current at the center, we get more details from a comparison with a straight line current in Chapter 2.

TABLE OF CONTENTS

CHAPTER 1

INTRODUCTION

1.1 Ionospheric currents at high latitudes

The auroral phenomenon is caused by energetic charged particles when they are bombarding the upper atmosphere at high latitudes. The light emission will thus be generated due to the change of energy levels from their excited energy states to the ground states. Direct rocket flights into aurora, however, have shown that electrons with energies of the order of $\cong$ 1 to 10 kev are the primary agency that excites aurora. Auroral displays occur frequently in a region of magnetic latitude $65^{\circ} \sim 70^{\circ}$ called auroral zone and less in middle and low latitudes during magnetically disturbed days. In such disturbed days, the auroral zone will advance toward the equator and retreat from the pole.

The energetic electrons are responsible for the enhancement of the geomagnetic activity called polar geomagnetic substorms. Birkeland [1908] attributed such substorms to large ionospheric circulating currents due to these electrons spiraling along the geomagnetic field lines. These currents supply a link connecting the low ionosphere and the outer part of the magnetosphere.

The most interesting and important feature in aurora is the auroral arc in which intense currents flow along or perpendicular to the arc. Those currents are called auroral electrojets in which the Hall currents are considered to be more important because they dominate most of the observed auroral-latitude magnetic activity.

1.2 Theoretical Mechanism and Observational Evidence

Magnetospheric mechanisms that produce field-aligned currents were first studied by Alfvén [1939, 1970, 1950], who considered the interaction of solar plasma streams with the geomagnetic field. He calculated particle-drift path in the earth's dipole magnetic field with superimposed uniform electric and magnetic fields. The differing drift paths of positive and negative particles causes a tendency for a charge separation layer to form at the inner edge of the convection region in the magnetosphere shown in the Fig. 3. The charge buildup in this layer called Alfvén layer is prevented by discharging Birkeland currents into the auroral ionosphere.

The merging of magnetic field lines across the neutral sheet in the geomagnetic tail causes a flow of plasma toward the earth. This was first suggested by Dungey [1961].

The thickness of the Alfvén layer is theoretically determined for monoenergetic electrons and ions to be between 10^2 meters for zero ionosphere conductivity and several earth radii for high ionospheric conductivity. For realistic ionospheric conductivities and breadth of particle spectra, an Alfvén layer about 2 R_e thick at its thickest point would seem a reasonable estimate. When the Alfvén layer moves inward into the plasma trough, transient electric fields aligned parallel to the magnetic field should be created. At such times, especially intense Birkeland currents would be generated, as described by M. A. Schield, J. W. Freeman, and A. J. Dessler [1969].

Kristian Birkeland in 1908 proposed that certain high-latitude magnetic perturbations were caused by a system of horizontal currents in

the upper atmosphere supplied by vertical (geomagnetically aligned) currents from above the atmosphere. Boström found two basic solutions, one in which a horizontal electrojet connects two filamentary Birkeland currents, and the other in which broad Birkeland sheet currents (Fig. 2) flow to the edges of the arc, with a transverse closing current and a Hall electrojet. In this thesis, we adopted a model similar to the second solution and assumed that the arc was bombarded by energetic precipitating electrons.

The electric current density in the ionosphere can be written

$$\vec{I} = \sigma_p \vec{E}_\perp + \sigma_h \vec{B} \times \vec{E}_\perp / |\vec{B}| + \sigma_\parallel \vec{E}_\parallel$$

The sign $\perp$ and $\parallel$ are used to denote components perpendicular and parallel to B. And σ_p, σ_h, and $\sigma_\parallel$ are the Pederson conductivity, the Hall conductivity and the conductivity parallel to B respectively. If we assume the B field in $\vec{Z}$ direction, we can write the current components as

$$I_x = \sigma_p E_x - \sigma_h E_y$$
$$I_y = \sigma_p E_y + \sigma_h E_x$$
$$I_z = \sigma_\parallel E_z$$

Boström had calculated these three conductivities as functions of height both for the undisturbed ionosphere surrounding the arc and for the region within the arc. He found the conductivity is at all heights much higher along the magnetic field lines than it is perpendicular to these. He derived that the final result of $\sigma_\parallel$ was about 30 mho/m and was then constant above 300 km and that the current $I_\parallel$ from about 95 km increased up to about 180 km and was then constant, about 2 amp/m.

Several rocket flights of a vector magnetometer system and energetic particle detectors have provided evidence for Birkeland sheet currents in association with individual auroral arcs, with a substantial fraction of the upward current carried by energetic precipitating auroral electrons within the arc [Cloutier et al., 1970; Park and Cloutier, 1971; Vondrak et al., 1971; Cloutier et al., 1973].

In the ionosphere, the transverse magnetic perturbations due to Birkeland sheet currents (we will call these currents as Birkeland currents afterwards for simplicity) cause very small change in field magnitude (smaller than 5 gammas in this thesis) and slight deflection in field direction (smaller than 1.1^{o}). Therefore unambiguous determination of the magnitude and spatial extent of Birkeland currents requires extremely precise in situ vector magnetic measurements by sounding rockets or satellites. The recent development by Cloutier [1969] of a rocket-borne magnetometer system capable of making precise ($\approx 0.01^{o}$) vector measurements has made it possible to investigate the phenomenon of field-aligned currents in the lower ionosphere.

The auroral arcs are generally so long that they stretch from horizon to horizon. Akasofu [1963] has given an example of a 5000-km-long arc. The thickness of homogeneous arcs has been measured by Kim and Volkman [1963] who have found values ranging from 3.5 - 18 km with a mean value of 9.1 km.

The sharply defined lower border of the arc is commonly at an altitude of 100 km to 120 km, corresponding to the approximate penetration depth of the 1 - 10 kev electrons. Hill [1965] has studied the luminosity-height relationship of aurorals at Fort Churchill irrespective

of auroral form, and found that the lower border was usually between 80 km and 150 km altitude with a maximum occurrence between 110 km and 120 km.

1.3 The purposes of this thesis

The purposes of this thesis were

(1) to study the magnetic perturbations near to or far from the electrojet flowing within an arc when a spatial fold develops in the arc;

(2) to study the magnetic perturbations near to or far from the Birkeland sheet currents with spatial fold; and

(3) to study the magnetic perturbations near to or far from the combination of (1) and (2).

By doing so, these results can be applied for interpreting past or future observational data.

1.4 Brief Description of the Payload

The rocket carries the payload which consists mainly of vector magnetometer, charged-particle detectors, lunar aspect sensor and accessory devices.

The vector magnetometer is an optical pumping cesium vapor type. The Lamar frequency is proportional to the total field. The proportional constant is 3.49854 Hz/gamma. Thus we can detect field magnitude smaller than 1 gamma. The field thus measured is a scalar field. We can convert to a vector magnetometer by using a bias coil system which can produce a uniform and stable bias field at the sensor. The current of the bias coil is carefully calibrated and is supplied by a highly precise power

regulator which maintains a field of about 10,000 gammas with a stability within 1 gamma. The output signal is therefore proportional to the vector sum of the ambient and bias magnetic fields. The magnetometer sensor is installed near the top of the payload in order to reduce stray fields.

The lunar aspect sensor is used for determining orientation of the payload by basically detecting the moon light. It is made of two slits with an angle of 31° and a photo-sensitive diode shielded by an aluminum mask. The aspect sensor is mounted with the symmetry axis of the mask parallel to the vehicle spin axis. As the payload rotates, the moon as viewed from the diode transits the slits and two voltage pulses are amplified. If the angle σ between the light rays and the symmetry axis is changed, the distance between the slit transit points also changes. The separation of these two voltage pulses also changes. According to these changes, we can determine orientation of the payload.

The charged-particle detectors is used to determine the net directional flux of charges parallel to the magnetic field, or the fraction of the field-aligned current carried by energetic auroral particles. More details have been discussed by Vondrak [1970].

The other devices include telemetry and power supply systems, and appropriate switching and control circuitry.

CHAPTER 2

MAGNETIC PERTURBATION DUE TO THE KINKED LINE CURRENT

2.1 Determination of the equation of the rocket flight path

Since we are interested in deriving the magnetic fields along a rocket flight path, we can establish an equation of this path similar to the rocket trajactory. We also like the path to pass over the electrojet in three cases, such as center electrojet, left-hand side electrojet and right-hand side electrojet. Figure 4 shows this kind of configuration. We chose an ecliptical path which satisfies three fixed space points A(y = -150 km, z=o), B(y = o, z = 200 km), and C(y = +150 km, Z = o). In this Figure, the center electrojet is located at the center "o", the left-hand electrojet at left-hand distance of 100 km from the center 'o', and the right-hand electrojet at right-hand distance of 100 km from 'o'. We will abbreviate these three electrojets to center, L.H.S. and R.H.S. electrojet afterwards. According to the above description, the equation thus chosen is

$$\frac{(Y + c)^2}{a^2} + \frac{(Z + d)^2}{b^2} = 1 \qquad (2\text{-}1)$$

where a = 5.0

b = 20.0/3.0

c = o or -5.0/3.0 or +5.0/3.0 for center, or L.H.S., or R.H.S. electrojet respetively

d = 10.0/3.0

The conventional values can be yielded by multiplying above values by 30 km since we have adopted each length in terms of the displacement thickness ℓ (ℓ = 30 km). We will also use this unit afterwards throughout

the whole calculations. Equation (2-1) is a very good approximation to the radar tracking data which was derived and published by NASA . The rocketwas number 18.112 launched from Poker Flats Rocket Range near Fairbanks in Alaska on February 24, 1972.

2.2 Derivation of the field equations

The vector potential of a line current I, as shown in Fig. 5A, is given by

$$\vec{A} = \frac{I}{c} \int_{-L}^{L} \frac{d\vec{\ell}}{|\vec{\gamma}-\vec{\gamma}'|} \qquad (2\text{-}2)$$

where $\vec{\gamma}$ and $\vec{\gamma}'$ are the vector positions outside and inside the current source respectively, and L is the integration limit (we assumed $L \gg 1$). After integration,

$$\vec{A} = (-)\frac{\hat{x}I}{c} \left[\ell n \left(x + \sqrt{x^2 + y^2 + Z^2}\right)\right]_{x+L}^{x-L} \qquad (2\text{-}3)$$

The current system we adopted in this thesis is a kinked electrojet having three current branches such as A_1, A_2, and A_3 as shown in Fig. 5B in which A_1 and A_2 have the same length of 2L each other and A_3 has the displacement thickness ℓ of 30 km and the value of L was 1000 ℓ. The total field components can be calculated by summing each contribution of A_1, A_2, and A_3 current branches. The results were included in the Appendix A.

There is an ambient magnetic field $\vec{B}_g$ which is the geomagnetic field at the vehicle position calculated with the Jensen and Cain [1962]

spherical harmonic expansion. This expansion gave the average vector field determined over a period of years. Therefore it does not represent the true field. It will be convenient in our calculations to let B_g denote the computed geomagnetic field not including the field produced by the currents of our model. The $\vec{B}_g$ we used has a magnitude of 50,000 gammas and points downward with geomagnetic dip angle of 80 degrees lying in the Y-Z plane. If the measured field $\vec{B}_T$ which is the vector summation of B_g and B_s, the difference field, ΔB, is defined by

$$\Delta\vec{B} = \vec{B}_T - \vec{B}_g$$

2.3 Interpretation of the calculated results

The various ΔB profiles are shown in Figure 6 to Figure 17, in which Figure 6 to Figure 9 are for the center electrojet, 10 to 13 for L.H.S. and 14 to 17 for R.H.S. In these charts, X component has the smallest amplitude comparing to other three cases and nearly negligible variation ($\approx$ 0.1 gamma) after X = 9 (i.e., X = 9 x 30 = 270 km). Therefore, after X = 9 the kinked electrojet has the same fields as the straight line current does. Because we are dealing with the kinked line current for our current model, the maximum values of X, and y for the center electrojet do not appear at the symmetry axis of Y = o, but shift to about Y $\cong$ 1 at X = o. After X = 9, the four cases look symmetry about the symmetry axis. This is what a straight line current behaves. As X increases, Y and Z components of ΔB seem constant. The comparison of the straight line current and the kinked electrojet, we found the maximum deviations between these two current systems were about 2 gammas

for Y, and 1 for Z and T at X = o and about o after X = 9. The maximum fields are about 1.6, 3.5, 9.3 and 8.0 for X, Y, Z, and T. The minimum are -0.15, -10, -8.5, and -9.8 gammas for X, Y, Z, and T, respectively. The form of X component looks like a concave shape, Y like a convex, T like one cycle of sine wave and Z also like one cycle of a sine wave except with 180^{o} out of phase compared to T.

For L.H.S. electrojet (Fig. 10-13), larger variations are found in left part of the curves. The maximum values are 1.91, 5.0, 6.6, and 13.3 gammas and minimum are -0.25, -12.2, -14.0, and -7.0 for X, Y, Z, and T, respectively. An interesting result in Z component, the minimum value of -14.0 gammas occurs at X = 3 and increases its value starting from this minimum value point. The largest deviations between the kinked and the straight line current systems are 2 gammas for Y, Z, and T at X = o and approaches to o after X = 9. The largest variation points shift to $Y \cong -1$ for X and Y and $Y \cong -2.5$ for Z and T.

For the R.H.S. electrojet, these have more larger variations because the trajectory is closer to the current source comparing to the L.H.S. electrojet. The points with the largest variation points occur at about $Y \cong 1.5$ for X and Y, and $Y \cong 2.4$ for Z and T. The maximum values are 3.4, 12.0, 17.1, and 5.8 gammas, and the minimum are -0.9, -13.8, -6.3, and -17.6 gammas for X, Y, Z, and T, respectively. Besides, the largest deviations between the two current systems are about 4 gammas for Y, Z, and T at X = o and near o at X = 9. From the above charts, the reason why we did not mention any deviation for X component of ΔB in these two current systems is that the straight line current flowing along X direction produces no any X component of the B field. So

the $(\Delta B)_X$ curves themselves are actually the deviations.

The previously mentioned coordinates, X, Y, and Z are coincident with the ground coordinates, east, north and vertical in which the ambient field B_g (geomagnetic field of 50,000 gammas) lies in the vertical north plane with an angle of 10^o to the vertical axis as shown in the Fig. 1 and Fig. 4.

CHAPTER 3

MAGNETIC PERTURBATIONS DUE TO THE BIRKELAND SHEET CURRENTS

3.1 Determination of B fields

For a long straight line with the current flowing out of the plane of the paper ($\vec{Z}$), the vector potential A will be the form

$$A_Z = \frac{I}{c} \int_{-P}^{+P} \frac{dZ'}{\sqrt{X^2 + y^2 + (Z-Z')^2}} \qquad (3\text{-}1)$$

where P is the integration limit and is assumed as infinity.

After integration, the result will be

$$A_Z \cong (-) \frac{2I}{c} \ell n\, \rho_o \;, \quad P \to \infty \qquad (3\text{-}2)$$

where

$$\rho_o = \sqrt{X^2 + y^2} \qquad (3\text{-}3)$$

The more details about this calculated procedures will be included in the Appendix B. For a thin current sheet of the width of d and of the surface current density J flowing in $\vec{Z}$ direction as shown in Fig. 18A, we have

$$dI = J\, d\, (dx')$$

The vector potential A can be rewritten as

$$A_Z = -\frac{2}{c} Jd \int_{-L}^{L} \ell n\, \rho\, dx' \qquad (3\text{-}4)$$

where

$$\rho = \sqrt{(x-x')^2 + y^2} \quad \text{and} \qquad (3\text{-}5)$$

L again is another integration limit as same value of 1000 ℓ. After integrating (3-4), it will come out the form of

$$A_Z = \frac{zJd}{c} \left[\frac{1}{2} \; H \; \ell n \; (H^2+y^2) - H + y \tan^{-1} \left(\frac{H}{y}\right)\right]_{H=x-L}^{H=x+L} \qquad (3\text{-}6)$$

The field again can be calculated by taking the curl of $\underline{A\hat{Z}}$. In this thesis, we have adopted the sheet current system as shown in Fig. 18B. We again can compute the total fields at a field point due to various current parts such as A_1, A_2, A_3, Area 1, and Area 2 just as we did previously for the electrojet.

Actually, the equations thus derived only are valid for the exterior region of the current source. For the interior regions, we include these results in the Appendix B. The length of A3 is again of the value of ℓ (ℓ = 30 km). We also assumed that d = ℓ.

3.2 Interpretation of the calculated results

After calculating the X, Y, and Z components of B fields, we can calculate the results in ground coordinates . The three component fields are shown in Fig. 19-Fig. 22 at four different values such as X = 1.0, 1.5, 2.0, and 4.0 (i.e., X = 30, 45, 60, and 120 km). The symbol TO, VO, NO, and EO represent for the total field base line value (= 5 x 10^4 gammas), vertical component field base line value (= -4.92450 x 10^4 gammas), north component field base line value (= 8.680 x 10^3 gammas)

and east component field base line value (= 0.0 gammas). In these four curves, the largest variations is the east component in which the maximum value is ≈ 641 gammas at X = 1.0 which is the boundary of the two sheets. Since the maximum magnitude of the east fields is always larger than the scale of our diagram (400 gammas), the E curve will continuously appear from the bottom side of the diagram.

At x = 1.0, where the rocket flies through A2 and then along the right-hand boundary of the kinked current sheet, E curve changes very rapidly and linearly. The variations between Y = 1 and Y = 2 are caused by the kinked section and N curve changes sharply at Y = o ($\approx$ 70γ) and at Y = 1.6 ($\approx$ 120γ) respective to NO base line value.

The partial N curve which lies in the left-hand side of the axis Y = 1 is mainly due to Area 2 and the remainder of the curve is mainly due to Area 1. The V curve only has slight variations which the maximum value is about 25γ at Y $\cong$ 1.5. In these four curves, the T curve has the smallest variations (less than $\approx 5\gamma$). Because the TO value we so chose, the T curve is justΔB curve. If we start from X = 1.0 to a larger distance away from the center, the N and V curves become smaller, T is almost unchanged, and E has a rapid change and has a different shape in the near zone. After X = 4.0, V keeps constant and N reduces to a value of 10 γ. E curve looks like a sharp pulse with highly linear variations. The one feature we should mention is that the changes of the maximum values of E are 641, 659, 658, and 640γ at X = 1.0, 1.5, 2.0, and 4.0, respectively among which the largest number of 659γ occurs between X = 1.0 and 2.0. This tendency of the maximum value change is caused by the current section other than section

A2 because if only A2 exists, the maximum value should occur at the mid-point along X axis for the current section A2. This value we have found has the value of $\approx 628\gamma$. (If the sections other than section A2 are absent, the maximum value at Y = 0 will be the mid-point of the total length of the sheet.)

CHAPTER 4

MAGNETIC PERTURBATIONS DUE TO THE COMBINATION OF THE ELECTROJET AND THE SHEET CURRENTS

4.1 Determination of the combined fields

Since the line current we have just discussed is in $\vec{B} \times \vec{E}$ direction ($\vec{B} = -|B|\hat{Z}$, $\vec{E} = |E|\hat{y}$), the line current is a Hall current. In Chapter 2, we have calculated the magnetic fields due to the electrojet in ground coordinates. We like to calculate the total fields due to the combination of the electrojet and the sheet currents.

Fig. 1 shows this kind of the combined current system. Also in Fig. 18B the electrojet is coincident with the common boundary between the two oppositely-directed current sheets. Since these two current systems are in the same coordinates, the combined field components can be calculated by summation of the corresponding field components of the electrojet and the sheet currents. Furthermore, we again convert these derived results in the ground coordinates.

4.2 Magnitude variations of magnetic fields

The component fields thus computed were plotted as shown in Figure 23-Figure 29. Figure 23-27 show the combined center system at the following five different kinds of distance such as x = 1.0, 1,6, 2.0, 6.0, 7.0, and Figure 28 shows the L.H.S. electrojet combined fields. In these charts, we can find that the combined fields are mainly produced by the sheet currents in the near zone but in the far zone (after x = 4), the T and V are dominated by the electrojet. Starting from x = 7 (Fig. 27), the N is dominated by the electrojet. Since E component produced by the electrojet is a negligibly small quantity as compared to the E component produced by the

sheet currents, the combined E field is mainly caused by the sheet currents all the way. This point of view can be obviously examined from the Figure 27 and from our early plotted charts Fig. 6-Fig. 9 of the electrojet in which the component fields due to sheet currents are absent except E component. At x = 9.0 the component field variations are entirely due to the Hall current except E component. For center electrojet, the curves are nearly the same as we discussed in Chapter 3 except a slight difference caused by the Hall current. Figure 28 shows the variations for the combined current system at x = 1.0. This Figure looks the same as the Fig. 23 which is the combined fields for the center combined current system. The flight path at the beginning portion is closer to our current model. After examining our early plotted charts Fig. 10-Fig. 13, for the L.H.S. electrojet and Fig. 19 for sheet current, we can easily see that this is just the summation result of the L.H.S. electrojet and the sheet currents. Therefore the difference of Fig. 28 from Fig. 19 is only caused by the electrojet. The reason we so compare the difference is that the magnetic field produced by the sheet current is only a function of y (not a function of Z). Consequently, no matter what the location of the sheet current is, the field profile should be the same. Again at x = 7 (not shown in the chart), the field components T, V, and N are dominated by the L.H.S. electrojet as the same we discussed for the combined center current system.

4.3 Determination of directional variations of the magnetic fields

After determining the scalar ambient field B_g, we can measure the polar angle θ between the rocket spin axis and the magnetic field. Fig. 29 shows this configuration. In this thesis, we assumed the rocket conning axis is coincident with the spin axis. The initial angle θ_o was equal to 45° since we assumed the initial $\vec{B}_g$, which has an angle 10° to the vertical axis, lies in the Z-Y plane.

One additional angle, analogous to the azimuthal angle ϕ in a standard spherical coordinate system, is needed to completely specify the ambient field in the rocket-based coordinate system. This angle is equivalent to an angle measured about the rocket spin axis from some reference direction, fixed in space in the rocket coordinates, to the ambient field vector. Fig. 29 also shows this angle ϕ. We count the angle from the Y-Z plane, where $\hat{B}_g$ and the rocket spin axis are in this plane, to the plane which contains $\hat{B}_t$ (the ambient field vector) and the rocket spin axis.

We will calculate the variation, $\Delta\theta$, defined by $\theta-\theta_o$ and the variation, $\Delta\phi$, defined $\phi-\phi_o$ (here $\phi = 0^\circ$). The details about the equation derivations are included in the Appendix C.

4.4 Interpretation of the calculated results of the field directional variations

Fig. 30 and Fig. 31 show the $\Delta\phi$ charts. And Fig. 32 shows the $\Delta\theta$ chart. In the Fig. 30, we plotted $\Delta\phi$ at $x = 1.0$ (solid curve) and $\Delta\phi$ at 1.6 (dashed curve). The maximum

angle ϕ variation is $\approx 1.0^{\circ}$ at the north range = 0. There is only a slight change for these two curves in the left-hand portion. But starting from range = 1 to the right-hand side. There is a big change about 0.2° at range = 1 and a less bigger change about 0.1° at range = 2. Beyond the region of the range $\cong -1$ and the range $\cong 2.5$, angle ϕ is very small (less than 0.03° in the left-hand curves of range -1 and less than 0.04° in the right-hand curves of the range of 3). The Fig. 31 shows $\Delta\phi$ at x = 2.0 (solid curve) and at x = 4.0 (dashed curve). These two curves are nearly the same looking except a small variation about less than 0.07° in the right-hand curves of the range of 0. From the above $\Delta\phi$ curves, the variations are attributed to the E component changes and are in the opposite direction to the rocket spinning direction. The Fig. 32 shows five curves of $\Delta\theta$ at x = 1.0, 1.6, 2.0, 2.6 and 4.0. The maximum values are $\approx 0.13^{\circ}$ at the range $\cong 1.5$ at $x = 1.0$, $\approx 0.06^{\circ}$ at the range $\cong 1.9$ at $x = 1.6$, $\approx 0.03^{\circ}$ at the range $\cong 2.0$ at $x = 2.0$ and negligibly small values at farther distance. The minimum values are $\approx -0.09^{\circ}$ at the range = 0.2 at x - 1.0, $\approx -0.06^{\circ}$ at the range = -0.2 at x - 1.6, $\approx -0.04^{\circ}$ at the range = -0.6 at x - 2.0, and negligibly small values at farther distance. The variations of θ are attributed to the V and N components changes.

CHAPTER 5
SUMMARY, CONCLUSIONS AND DISCUSSION

Starting from X = 9.0, the kinked line current has been found having the same contributions to the magnetic field as the straight line current does, and the east component is negligibly small (0.3γ, Fig. 6 - F17). The magnitude of east component field has the smallest value (center: < 2γ, ≈ 20% of N and V, ≈ 25% of T; L.H.S.: < 2γ, ≈ 16% of N, ≈ 15% of V, and ≈ 30% of T; R.H.S.: < 3.5γ of N, ≈ 20% of V and T) at x = 1.0.

Starting from x = 4.0, the sheet current system has been found having a very slight magnetic field variations, ≈ 5γ for the total field (T), ≈ 0γ for the vertical component (V), ≈ 10γ for the north component (N) except for the E variations which were very rapidly and linearly (Fig. 19-Fig. 22).

The fields generated by the sheet current were independent on the altitude of the rocket flight path but were dependent on the horizontal range of the path.

The combined fields of the electrojet and the sheet current were dominated by the sheet current in the near zone (less than x - 4.0), but were dominated by the electrojet afterwards (starting from x = 4.0) except the E component (Fig. 23-Fig. 28).

The maximum value of $\Delta\phi$ was ≈ -1.0° for all the distance x which we explained that the '-' sign was opposite to directional change of the rocket spinning sense and was attributed to E component changes. Starting from x = 4.0, the changes of ϕ were highly linear (Fig. 30 and Fig. 31).

The maximum value of $\Delta\theta$ was $\approx 0.13^{\circ}$ and the minimum value was $\approx -0.09^{\circ}$ at x = 1.0 near zone. They were attributed to the V, N component changes. After x = 4.0, $\Delta\theta$ was negligibly small (Fig. 32).

The electrojet has a very little contribution to the ϕ and θ changes compared to the sheet current.

In Chapter 4, we have discussed the variations of the field direction ϕ and θ. But in Chapter 2 or Chapter 3, we did not mention anything about these variations. The reason was the $\Delta\phi$ and $\Delta\theta$ were dominated by the sheet currents as we stated in Chapter 4; and the electrojet had a negligibly contribution to them. Therefore, the $\Delta\phi$ and $\Delta\theta$ profiles for the electrojet were too small to be examined and the profiles for the sheet currents, were as the same as those of the combined field.

Let us describe more clearly. At the far zone (starting from x = 4.0) where the N and V components were very small for the sheet currents but were dominated by the electrojet, we found that there were no clear variations of θ. Furthermore, the E field was extremely small for the electrojet (Fig. 6-Fig. 9) compared to that of the sheet currents all the way. Therefore, $\Delta\phi$ can be explained only caused by the sheet currents.

In the Chapter 2, we have mentioned something about the rocket flight path. Fig. 33 shows the comparison of our model trajectory to the rocket trajectory. The symbol 'M' stands for the model trajectory using eq. (2-1) and the symbol 'R' stands for the rocket flight path. We have raised the level of this rocket trajectory up 15 km for comparison reason. The rocket trajectory was found using the equations (see the

Appendix D) which were derived by Mr. Jean Sesiano and Mr. Ray Casserly in Rice University. After applying these equations, we have found that our calculated data was pretty close to the NASA data (the maximum deviation less than ± 0.5-km). The field results along this rocket trajectory should be the same as those using our model trajectory beacuse

1) the fields produced by the sheet currents are independent on the altitudes, and

2) the fields produced by the electrojet have negligibly small errors for the field point so distant away from the current source ($\approx$ 4% deviations between the two apogees).

APPENDIX A

DERIVATION OF THE B FIELD EQUATIONS (LINE CURRENT)

The vector potential of a line current I flowing along $\vec{\ell}$ direction from -L to +L shown in Fig. 5A is given by

$$\vec{A} = \frac{I}{c} \int_{-L}^{L} \frac{d\vec{\ell}}{|\vec{\gamma}-\vec{\gamma}'|} \qquad \text{(A-1)}$$

where

L = integration limits

$\vec{\gamma}$ = vector position outside the current source

$\vec{\gamma}'$ = vector position of the current source

The current system we adopted in this thesis is a kinked electroject having three current branches, A_1, A_2, and A_3, shown in Fig. 5B in which A_1, and A_2 have the same length of 2L each other and A_3 has the displacement thickness ℓ with the current I flowing along $-\hat{y}$ direction.

For the current branch A_2 with a current I flowing along $\hat{x}$ direction from o to 2L, we have

$$d\vec{\ell} = \hat{x}\, dx'$$

$$|\vec{\gamma}-\vec{\gamma}'| = [\,(x-x')^2 + y^2 + Z^2\,]^{1/2}$$

After integration from o to 2L, we will get the following result

$$A_{XA2} = -\frac{I}{c}\,[\,\ell n\,(x-2L + \sqrt{(x-2L)^2 + y^2 + Z^2}) - \ell n\,(x + \sqrt{x^2 + y^2 + Z^2})\,] \qquad \text{(A-2)}$$

The components of the magnetic field can be derived by taking the curl of (A-2). They were

$$B_x = 0$$

$$B_{yA2} = \frac{\partial Ax}{\partial Z} = -\frac{IZ}{c}\left[\frac{1}{(x-2L)\sqrt{(x-2L)^2 + y^2 + Z^2} + (x-2L)^2 + y^2 + Z^2}\right.$$

$$\left. - \frac{1}{x\sqrt{x^2 + y^2 + Z^2} + x^2 + y^2 + Z^2}\right] \qquad (A-3)$$

$$B_{ZA2} = \frac{\partial Ax}{\partial Y} = \frac{IY}{c}\left[\frac{1}{(-x+2L)\sqrt{(x-2L)^2 + y^2 + Z^2} + (x-2L)^2 + y^2 + Z^2}\right.$$

$$\left. - \frac{1}{x\sqrt{x^2 + y^2 + Z^2} + x^2 + y^2 + Z^2}\right] \qquad (A-4)$$

Similarly we can derive the field components due to branch A3 and A1. They were

$$B_{XA3} = \frac{-\partial AY}{\partial Z} = -\frac{IZ}{c}\left[\frac{1}{Y\sqrt{x^2 + y^2 + Z^2} + x^2 + y^2 + Z^2} - \right.$$

$$\left. \frac{1}{(y-\ell)\sqrt{(y-\ell)^2 + X^2 + Z^2} + x^2 + (y-\ell)^2 + Z^2}\right]$$

$$B_{YA3} = 0$$

$$B_{ZA3} = \frac{\partial A_y}{\partial X} = \frac{Ix}{c} \left[\frac{1}{Y\sqrt{x^2 + y^2 + Z^2} + x^2 + y^2 + Z^2} \right.$$

$$\left. - \frac{1}{(y-\ell)\sqrt{x^2 + (y-\ell)^2} + X^2 + (y-\ell)^2 + Z^2} \right]$$

(A-5)

and

$$B_{XA1} = 0$$

$$B_{yA1} = \frac{\partial A_x}{\partial Z} = \frac{IZ}{c} \left[\frac{1}{x\sqrt{x^2 + (y-\ell')^2 + Z^2} + x^2 + (y-\ell)^2 + Z^2} \right.$$

$$\left. - \frac{1}{(x+2L)\sqrt{(x+2L)^2 + (y-\ell)^2 + Z^2} + (x+2L)^2 + (y-\ell)^2 + Z^2} \right]$$

$$B_{ZA1} = \frac{-\partial A_x}{\partial y} = \frac{I}{c}(y-\ell) \left[\frac{1}{x\sqrt{x^2 + (y-\ell)^2 + Z^2} + x^2 + (y-\ell)^2 + Z^2} \right.$$

$$\left. - \frac{1}{(x+2L)\sqrt{(x+2L)^2 + (y-\ell)^2 + Z^2} + (x+2L)^2 + (y-\ell)^2 + Z^2} \right]$$

(A-6)

In the above equations, we adopted a quite general form for any length of the electrojet. The integration limits L can be chosen for any value. In this thesis, we have chosen the value L of 1000 ℓ in all of our calculations. The displacement ℓ is also changeable to any value. We chose ℓ equal to 30 km in our calculations.

Therefore, the field compnents at the particular point along the trajectory due to A_1, A_2, and A_3 current branches are just as follows:

$$B_X = B_{xA1} + B_{xA2} + B_{xA3}$$

$$B_y = B_{yA1} + B_{yA2} + B_{yA3} \qquad \text{(A-7)}$$

$$B_Z = B_{ZA1} + B_{ZA2} + B_{ZA3}$$

According to these results, we can calculate any fields at any points by substituting the values of X, Y, and Z (all are in terms of ℓ) in our computer performance. The quantities (in terms of 30 km) we thus used is to reduce the size of the real number for computer calculations.

APPENDIX B

DETERMINATION OF B FIELD EQUATIONS (SHEET CURRENTS)

For a long straight wire with current flowing out of the plane of the paper ($\vec{Z}$), the vector potential can be written as

$$A_Z = \frac{I}{c} \int_{-P}^{P} \frac{dZ'}{\sqrt{x^2 + y^2 + (Z-Z')^2}} \qquad \text{(B-1)}$$

where P is the integration limit and this time we assume P approaches to infinity.

This time we will use some different techniques since we are dealing with the infinite value of P. After integration from -P to P, eq. (B-1) will become

$$A_Z = (-)\frac{I}{c} \left\{ \ell n \left(\omega + \sqrt{x^2 + y^2 + \omega^2} \right) \right\}_{Z+P}^{Z-P} \qquad P \to \infty$$

$$= (-)\frac{I}{c} \left\{ \ell n \left[\frac{(Z-P) + \sqrt{x^2 + y^2 + (Z\ P)^2}}{(Z+P) + \sqrt{x^2 + y^2 + (Z+P)^2}} \right] \right\} \qquad \text{(B-2)}$$

After being divided both the numerator and the denominator by P in the bracket of the logarithm, we will get

$$A_Z \cong (-)\frac{I}{c} \left\{ \ell n \left[\frac{(\frac{Z}{P} - 1) + \sqrt{\frac{x^2+y^2}{P^2} + 1 - \frac{2Z}{P}}}{(\frac{Z}{P} + 1) + \sqrt{\frac{x^2+y^2}{P^2} + 1 + \frac{2Z}{P}}} \right] \right\}$$

$$\cong (-)\frac{I}{c}\left\{ \ell n\left[\frac{\left(\frac{Z}{P}-1\right)+1+\frac{1}{2}\left(\frac{\rho_o^2}{P^2}-\frac{2Z}{P}\right)}{\left(\frac{Z}{P}+1\right)+1+\frac{1}{2}\left(\frac{\rho_o^2}{P^2}+\frac{2Z}{P}\right)} \right] \right\} \quad , \text{(where } \rho_o = \sqrt{x^2+y^2}\text{)}$$

$$\cong \frac{I}{c}\ \ell n\ \left[\frac{4P^2}{\rho_o^2}+1+\frac{4PZ}{\rho_o^2}\right] \qquad \text{(B-3)}$$

Since $P^2 >>> x^2 + y^2$, A_Z can be rewritten as

$$A_Z \cong \frac{I}{c}\ \ell n\ \left(\frac{4P^2}{x^2+y^2}\right)$$

$$\cong (-)\frac{2I}{c}\ \ell n\ \rho_o \qquad \text{(B-4)}$$

where $\rho_o = \sqrt{x^2+y^2}$

We have omitted the constant term $\frac{I}{c}\ \ell n(4P^2)$ from the right-jand side of eq. (B-4) because

1.) when $P \to \infty$, A_Z will approach to ∞ and this is an irrelevant result since they drop out on differenciation, and

2.) eq. (B-4) is correct in that on calculating B from it, using $\vec{B} = \vec{\nabla} \times \vec{A}$.

For a thin current sheet of the width of d, and of the surface current density J flowing in $\vec{Z}$ direction as shown in Fig. 18A, we have $dI = Jd(dx')$. The vector potential A can be rewritten as

$$A_Z = -\frac{2}{c} Jd \int_{-L}^{L} \ell n\ \rho\ dx' \qquad \text{(B-5)}$$

where

$$\rho = \sqrt{(x-x')^2 + y^2} \qquad \text{(B-6)}$$

and L again is the integration limit.

After integrating eq. (B-5) from -L to +L, we yield

$$A_Z = \frac{2Jd}{c} \left\{ \frac{1}{2} X\ \ell n(X^2 + y^2) - X + y \tan^{-1}\left(\frac{X}{y}\right) \right\}_{X = x+L}^{X = x-L} \qquad \text{(B-7)}$$

The field components are calculated by taking the curl of (B-7). They are

$$B_x = \frac{2Jd}{c} \left\{ \tan^{-1}\left(\frac{x-L}{y}\right) - \tan^{-1}\left(\frac{x+L}{y}\right) \right\} \qquad \text{(B-8)}$$

$$B_y = \frac{Jd}{c}\ \ell n \left\{ \frac{(x+L)^2 + y^2}{(x-L)^2 + y^2} \right\} \qquad \text{and} \qquad \text{(B-9)}$$

$$B_Z = 0$$

Likewise, we can use this method to calculate the fields of a current sheet in a coordinates rotated with an angle of 90^o in a counter-clock wise direction with respect to the coordinates X, Y, Z as shown in Fig. 18A. The vector potential thus becomes

$$A_Z = \frac{2Jd}{c} \left[\frac{1}{2} Y \ell n \, (x^2+Y^2) - Y + x \tan^{-1} \left(\frac{Y}{x}\right) \right]_{Y1}^{Y2} \qquad \text{(B-10)}$$

where

$$Y1 = y + \frac{\ell}{2} \quad \text{and}$$

$$Y2 = y - \frac{\ell}{2}$$

The component fields thus computed by integrating from $-\frac{\ell}{2}$ to $+\frac{\ell}{2}$ are

$$B_x = (-) \frac{Jd}{c} \ell n \left[\frac{x^2 + (y + \frac{\ell}{2})^2}{x^2 + (y - \frac{\ell}{2})^2} \right] \qquad \text{(B-11)}$$

$$B_y = (-) \frac{2Jd}{c} \left\{ \tan^{-1} \frac{1}{x} (y - \frac{\ell}{2}) - \tan^{-1} \frac{1}{x} (y + \frac{\ell}{2}) \right\} \qquad \text{(B-12)}$$

$$B_Z = 0$$

For a sheet current system as shown in Fig. 18B, we have divided our sheet current model into five parts, such as A1, A2, A3, Area 1 and Area 2 in which A1 and A2 have the same size with the same length of 2L each other as line current model, so do Area 1 and Area 2 except the current flowing only in one direction in each of them which the current flows in $\vec{Z}$ for area 1 and in $-\vec{Z}$ for area 2. Each of A1, A2, and A3 has two oppositely-directed currents flowing on two sides of the common boundary,

and Area 1 and Area 2 have only one directional current flowing through each of them.

We can use the eq. (B-8) and eq. (B-9) to calculate the fields components due to A1, A2, and those due to Area 1 and Area 2 by coordinate transformation method and eq. (B-11) and eq. (B-12) can be used likewise to calculate B yields due to A3. Actually, the equations thus derived only are valid in the outside region (outside of the current source of the sheets). If the field points to be measuring locate inside the current source, we should reconsider this sheet having two parts. These two parts are the upper part (the portion above the point) and the lower part (the portion below the point). Each of the two parts has a different contribution to the B field. Fig. 18B shows such a point. But we have chosen this point located at x axis for convenience.

The final results thus derived in each of the current parts for either outside or inside region as shown in Fig. 18B were given by the exterior region of the current source $|y| > d$

$$B_{xa1} = (-)\frac{2Jd}{c}\left\{\tan^{-1}\left(\frac{x+2L+d}{Y-\ell-\frac{d}{2}}\right) - \tan^{-1}\left(\frac{x+d}{Y-\ell-\frac{d}{2}}\right) - \tan^{-1}\left(\frac{x+2L+d}{Y-\ell+\frac{d}{2}}\right) + \tan^{-1}\left(\frac{x+d}{Y-\ell+\frac{d}{2}}\right)\right\}$$

$$B_{xa2} = (-)\frac{2Jd}{c}\left\{\tan^{-1}\left(\frac{x-d}{Y-\frac{d}{2}}\right) - \tan^{-1}\left(\frac{x-2L-d}{Y-\frac{d}{2}}\right) - \tan^{-1}\left(\frac{x-d}{Y+\frac{d}{2}}\right) + \tan^{-1}\left(\frac{x-2L-d}{Y+\frac{d}{2}}\right)\right\}$$

$$B_{xa3} = (-)\frac{2Jd}{c}\left\{\frac{1}{2}\ell n\ \frac{\left[(x-\frac{d}{2})^2 + y^2\right]\ \left[(x+\frac{d}{2})^2 + (y-\ell)^2\right]}{\left[(x-\frac{d}{2})^2 + (y-\ell)^2\right]\left[(x+\frac{d}{2})^2 + y^2\right]}\right\}$$

$$B_{xarea1} = (-)\frac{2Jd}{c}\left\{\tan^{-1}\left(\frac{x+d}{y-\ell-\frac{d}{2}}\right) - \tan^{-1}\left(\frac{x-d}{y-\ell-\frac{d}{2}}\right)\right\}$$

$$B_{xarea2} = (-)\frac{2Jd}{c}\left\{-\tan^{-1}\left(\frac{x+d}{y+\frac{d}{2}}\right) + \tan^{-1}\left(\frac{x-d}{y+\frac{d}{2}}\right)\right\}$$

$$B_{ya1} = (-)\frac{2Jd}{c}\left\{\frac{1}{2}\ell n\ \frac{\left[(x+2L+d)^2 + (y-\ell+\frac{d}{2})^2\right]\ \left[(x+d)^2 + (y-\ell-\frac{d}{2})^2\right]}{\left[(x+d)^2 + (y-\ell+\frac{d}{2})^2\right]\ \left[(x+2L+d)^2 + (y-\ell-\frac{d}{2})^2\right]}\right\}$$

$$B_{ya2} = (-)\frac{2Jd}{c}\left\{\frac{1}{2}\ell n\ \frac{\left[(x-d)^2 + (y+\frac{d}{2})^2\right]\ \left[(x-2L-d)^2 + (y-\frac{d}{2})^2\right]}{\left[(x-2L-d)^2 + (y+\frac{d}{2})^2\right]\left[(x-d)^2 + (y-\frac{d}{2})^2\right]}\right\}$$

$$B_{ya3} = (-)\frac{2Jd}{c}\left\{\tan^{-1}\left(\frac{y-\ell}{x-\frac{d}{2}}\right) - \tan^{-1}\left(\frac{y}{x-\frac{d}{2}}\right)\right] - \tan^{-1}\left(\frac{y-\ell}{x+\frac{d}{2}}\right) - \tan^{-1}\left(\frac{y}{x+\frac{d}{2}}\right)\right\}$$

$$B_{yarea1} = (-)\frac{2Jd}{c}\left\{\frac{1}{2}\ell n\ \frac{(x-d)^2 + (y-\ell-\frac{d}{2})^2}{(x+d)^2 + (y-\ell-\frac{d}{2})^2}\right\}$$

$$B_{yarea2} = (-)\frac{2Jd}{c}\left\{-\frac{1}{2}\ell n\ \frac{\left[(x-d)^2 + (y+\frac{d}{2})^2\right.}{(x+d)^2 + (y+\frac{d}{2})^2}\right\}$$

The interior region of the current source $\ell - d \leq y \leq \ell + d$

for al $B_{xal} = (B_{xal})_{d-|y|} + (B_{xal})_{|y|} + (B_{xal})_s$

where

$$B_{xal}\Big|_{d-|y|} = \frac{2J}{c}(d-|y-\ell|)\left\{\tan^{-1}\frac{Z+2L+d}{\frac{d-|y-\ell|}{2}} - \tan^{-1}\frac{x+d}{\frac{d-|y-\ell'|}{2}}\right\}$$

$$B_{xal}\Big|_{|y|} = (-)\frac{2J}{c}|y-\ell|\left\{\tan^{-1}\frac{x+2L+d}{\frac{|y-\ell|}{c}} - \tan^{-1}\frac{x+d}{\frac{|y-\ell|}{2}}\right\}$$

$$B_{xal}\Big|_{s} = \frac{2Jd}{c}\left\{\tan^{-1}\frac{x+2L+d}{|y-\ell|+\frac{d}{2}} - \tan^{-1}\frac{x+d}{|y-\ell|+\frac{d}{2}}\right\}$$

$$B_{yal} = q\frac{J}{c}\left\{(d-|y-\ell|)\ln\left[\frac{(x+d)^2 + (d-|y-\ell|)^2/4}{(x+2L+d)^2 + (d-|y-\ell|)^2/4}\right] + \right.$$

$$\left. |y-\ell|\ln\left[\frac{(x+d)^2 + (y-\ell)^2/4}{(x+2L+d)^2 + (y-\ell)^2/4}\right] - d\ln\left[\frac{(x+d)^2 + (|y-\ell|+\frac{d}{2})^2}{(x+2L+d)^2 + (|y-\ell|+\frac{d}{2})^2}\right]\right\}$$

$B_{yal} = 0$ at $y - \ell = 0$

where $q = +1$ for the field point in the upper current sheet and $q = -1$ in the lower current sheet.

the subscript 'd-|y|' stands for the partial section with the width of '$d-|y|$'

the subscript $|y|$ stands for the partial section with the width of '$|y|$'

the subscript s stands for the other unoccupied current sheet (in this case, the field point is located at the exterior region of the current source count from the common boundary)

for a2, $|y| \leq d$

$$B_{xa2} = (B_{xa2})_{d-|y|} + (B_{xa2})_{|y|} + (B_{xa2})_s$$

where

$$B_{xa1}\Big|_{d-|y|} = \frac{2J}{c}(d-|y|)\{\tan^{-1}(\frac{x-d}{\frac{d-|y|}{2}}) + \tan^{-1}(\frac{2L+d-x}{\frac{d-|y|}{2}})\} =$$

due to the sheet of the width $d-|y|$

$$B_{xa2}\Big||y| = (-)\frac{2J}{c}|y|\{\tan^{-1}\frac{2(x-d)}{|y|} + \tan^{-1}\frac{2(2L+d-x)}{|y|}\} =$$

due to the sheet of the width $|y|$

$$B_{xa2}\Big|_s = q\frac{2Jd}{c}\{\tan^{-1}(\frac{x-d}{|y|+\frac{d}{2}}) + \tan^{-1}(\frac{2L+d-x}{|y|+\frac{d}{2}})\} =$$

due to another source current sheet

$$B_{ya2} = q\frac{J}{c}\left\{(-d+|y|)\ell n\left[\frac{(x-2L-d)^2 + (\frac{d-|y|}{2})^2}{(x-d)^2 + (\frac{d-|y|}{2})^2}\right] - |y|\ \ell n\right.$$

$$\left.\left[\frac{(x-2L-d)^2 + \frac{y^2}{4}}{(x-d)^2 + \frac{y^2}{4}}\right] + d\ \ell n\left[\frac{(x-2L-d)^2 + (|y| + \frac{d}{2})^2}{(x-d)^2 + (|y| + \frac{d}{2})^2}\right]\right\}$$

$$B_{ya2} = 0 \text{ at } y = 0,\ x = x$$

for areal, $\ell \leq y \leq \ell + d$

$$B_{xareal} = (B_{xareal})_{d-y} + (B_{xareal})_{y}$$

$$B_{xareal}\Big|_{y} = (-)\frac{2J}{c}(y-\ell)\left\{\tan^{-1}\frac{2(x+d)}{y-\ell} - \tan^{-1}\frac{2(x-d)}{y-\ell}\right\}$$

$$B_{yareal} = (-)\frac{J}{c}\left\{(y+\ell+d)\ \ell n\left[\frac{(x-d)^2 + (y-\ell-d)^2/4}{(x+d)^2 + (y-\ell-d)^2/4}\right] +\right.$$

$$\left.(y-\ell)\ \ln\left[\frac{(x-d)^2 + (y-\ell)^2/4}{(x+d)^2 + (y-\ell)^2/4}\right]\right\}$$

for area2, $-d \leq y \leq 0$

$$B_{x\text{area2}} = (B_{x\text{area2}})_{d-y} + (B_{x\text{area2}})_{y}$$

where

$$B_{x\text{area2}}\Big|_{d-y} = \frac{2Jy}{c}\left\{-\tan^{-1}\frac{2(x+d)}{y} + \tan^{-1}\frac{2(x-d)}{y}\right\}$$

$$B_{x\text{area2}}\Big|_{y} = \frac{2J}{c}(y+d)\left\{\tan^{-1}\frac{2(x+d)}{y+d} - \tan^{-1}\frac{2(x-d)}{y+d}\right\}$$

$$B_{y\text{area2}} = \frac{J}{c}\left\{-y\,\ell n\left[\frac{(x-d)^2 + \frac{y^2}{4}}{(x+d)^2 + y^2/4}\right] + (y+d)\ell n\left[\frac{(x-d)^2 + (y+d)^2/4}{(x+d)^2 + (y+d)^2/4}\right]\right\}$$

In the above results, we did not consider the interior region of A3 since we assumed the trajectory did not penetrate this region. Therefore the field results due to A3 are only considered as for the outside region. In these equations, the value L we adopted was 1000 ℓ (ℓ = 30 km) as we did for the kinked electrojet. And we also used the value of d equal to the displacement thickness ℓ for our sheet current model.

APPENDIX C

DETERMINATION OF THE EQUATIONS OF THE FIELD DIRECTIONAL CHANGES

After determining the magnitudes of B_t (the measured total field) and B (the field produced by the current model), we can calculate the angle β (Fig. 29) by using the equation

$$B^2 = B_g^2 + B_t^2 - 2B_g B_t \cos \beta$$

or

$$\beta = \cos^{-1} \left[\frac{B_g^2 + B_t^2 - B^2}{2B_g B_t} \right] \text{ (for a plane triangle)} \qquad \text{(C-1)}$$

where B_g is assumed as our initial ambient field (=50,000γ) with an angle of $10^\bullet$ to the vertical axis.

In the Figure, $\theta_o = 35^\bullet$, $\alpha_o = 10^\bullet$ and α can be computed by the equation

$$B_t \cos \alpha = -B_v$$

or

$$\alpha = \cos^{-1} \left(\frac{-B_v}{B_t} \right) \qquad \text{(C-2)}$$

where

B_v is the magnitude of the vertical component field. The "-" sign is used to calculate the complementary angle of the angle Ⓗ cartisian coordinate. Use the calculated α and β, and known initial values α_o and θ_o. In the spherical triangle ΔEFH, the angle C can be found using the equation of the spherical law of cosines.

$$C = \cos^{-1} \left[\frac{- \cos \beta \cos \alpha_o + \cos \alpha}{\sin \beta \sin \alpha_o} \right] \qquad \text{(C-3)}$$

In the spherical triangle ΔGFH, the θ can be found using

$$\theta = \cos^{-1} [\cos \theta_o \cos\beta + \sin \theta_o \sin \beta \cos c] \quad \text{(C-3)}$$

$$\Delta\theta = \theta - \theta_o \quad \text{(C-4)}$$

Use this calculated θ to calculate the following angle ϕ.

In the same triangle ΔGFH, the angle ϕ can be found using the equation of the spherical law of sines

$$\phi = \sin^{-1} \left(\frac{\sin \beta \ \sin c}{\sin \theta} \right) \quad \text{(C-5)}$$

$$\Delta\phi = \phi - \phi_o$$

where the initial value ϕ_o equals to 0^o.

APPENDIX D

Determination of the rocket trajectory

After calculating the longitudes and the latitudes by using

$$LONG = A0LO + A1LO \times T + A2LO \times T^2 + A3LO \times T^3 \qquad (D\text{-}1)$$

$$LAT = A0LA + A1LA \times T + A2LA \times T^2 + A3LA \times T^3 + A4LA \times T^4 \qquad (D\text{-}2)$$

where T= flight time

LONG=longitude in degrees

LAT= latitude in degrees and

other quantities are constants,

we plug in the range (Km) PER DEGREE OF THE LATITUDE, 113.2259 Km / lat., and R_e to calculate the N-S range and E-W range respect to a reference point located on the surface of the earth. We then convert to the horizontal range by

$$\left((NS)^2 + (EW)^2 \right)^{1/2}$$

In this thesis, we assume the plane of the trajectory was in the Y-Z plane (or V-N plane). Eq(D-1) and Eq(D-2) were derived by Jean Sesiano and Ray Casserly. The altitude can be computed using

$$ALTITUDE = HA - C1 \times (T-TA)^2 - C2 \times (T-TA)^4 \qquad (D\text{-}3)$$

where altitude is in Km

HA=apogee (Km)

TA=flight time (sec.) at the apogee and

C1 and C2 are constants.

This trajectory was plotted in the Fig.33 using the symbol 'R'.

note: We have changed a slight values about the constants such as HA, TA, A0LO and A0LA in order to obtain the results coincident with the NASA published data. The error compared to the NASA data was found less than $\pm$0.5 Km.

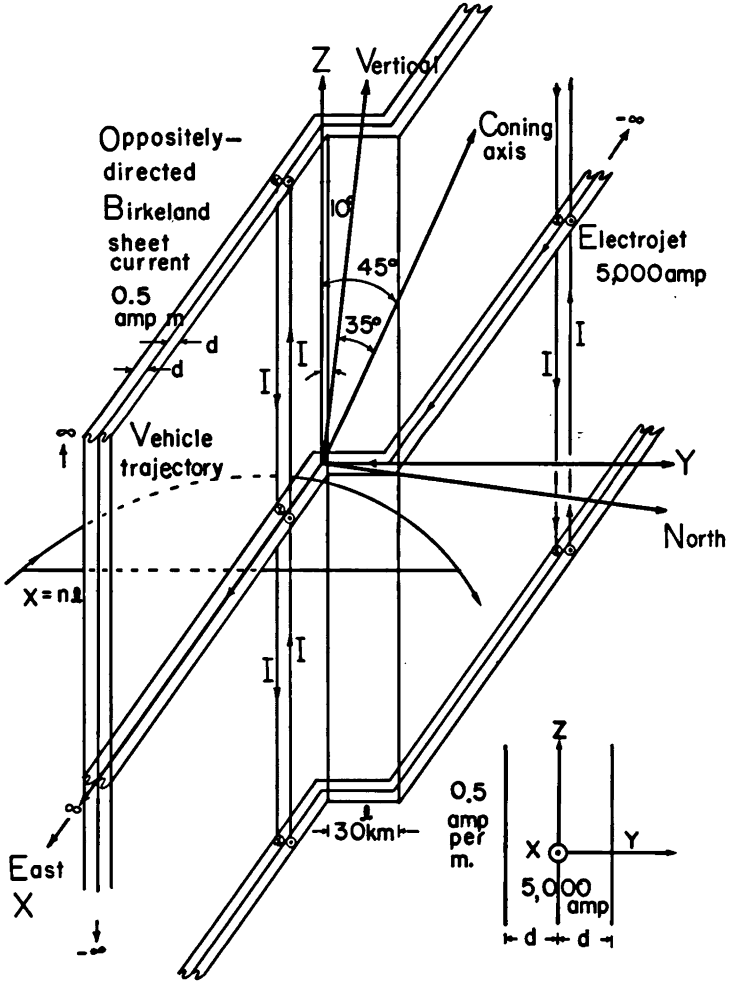
Z
Vertical
Oppositely-directed Birkeland sheet current 0.5 amp m
d
d
10°
45°
35°
Coning axis
-∞
Electrojet 5,000 amp
I
I
I
I
I
I
∞
Vehicle trajectory
Y
North
X = nΔ
30km
East
X
-∞
0.5 amp per m.
Z
X
Y
5,000 amp
d
d

FIGURE 1

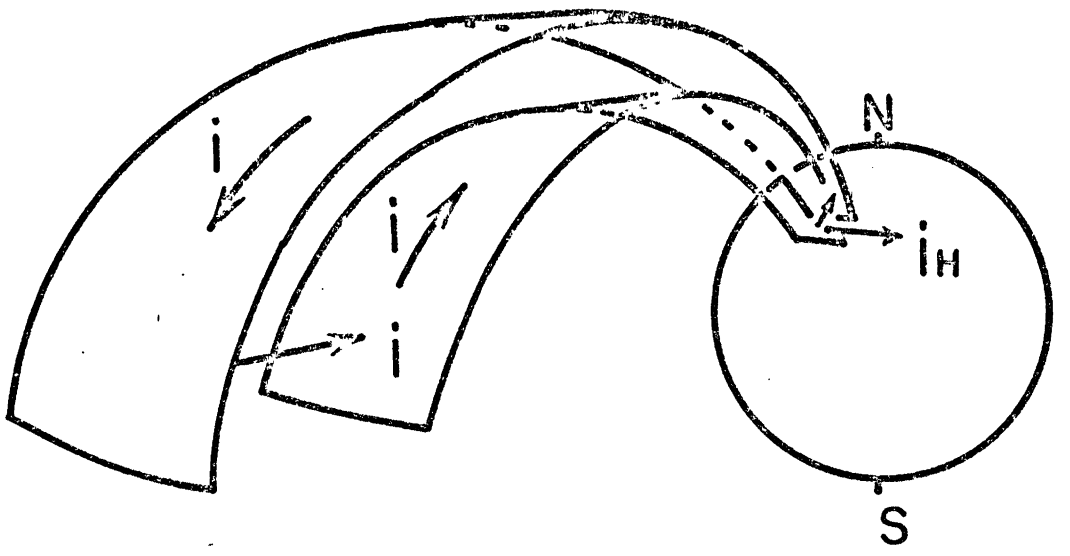

FIGURE 2

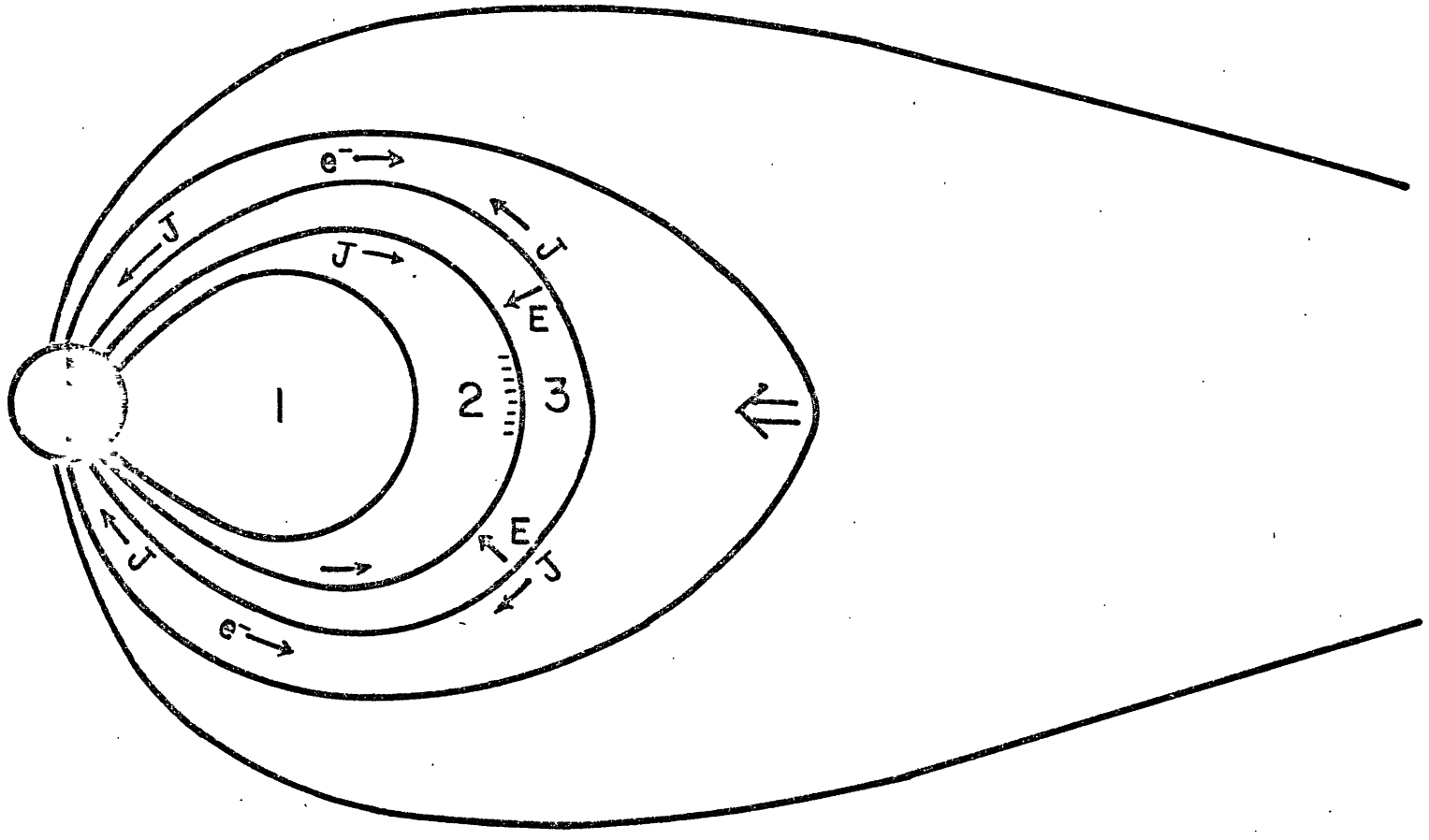

1. PLASMASPHERE
2. PLASMATROUGH
3. ALFVEN LAYER

FIGURE 3

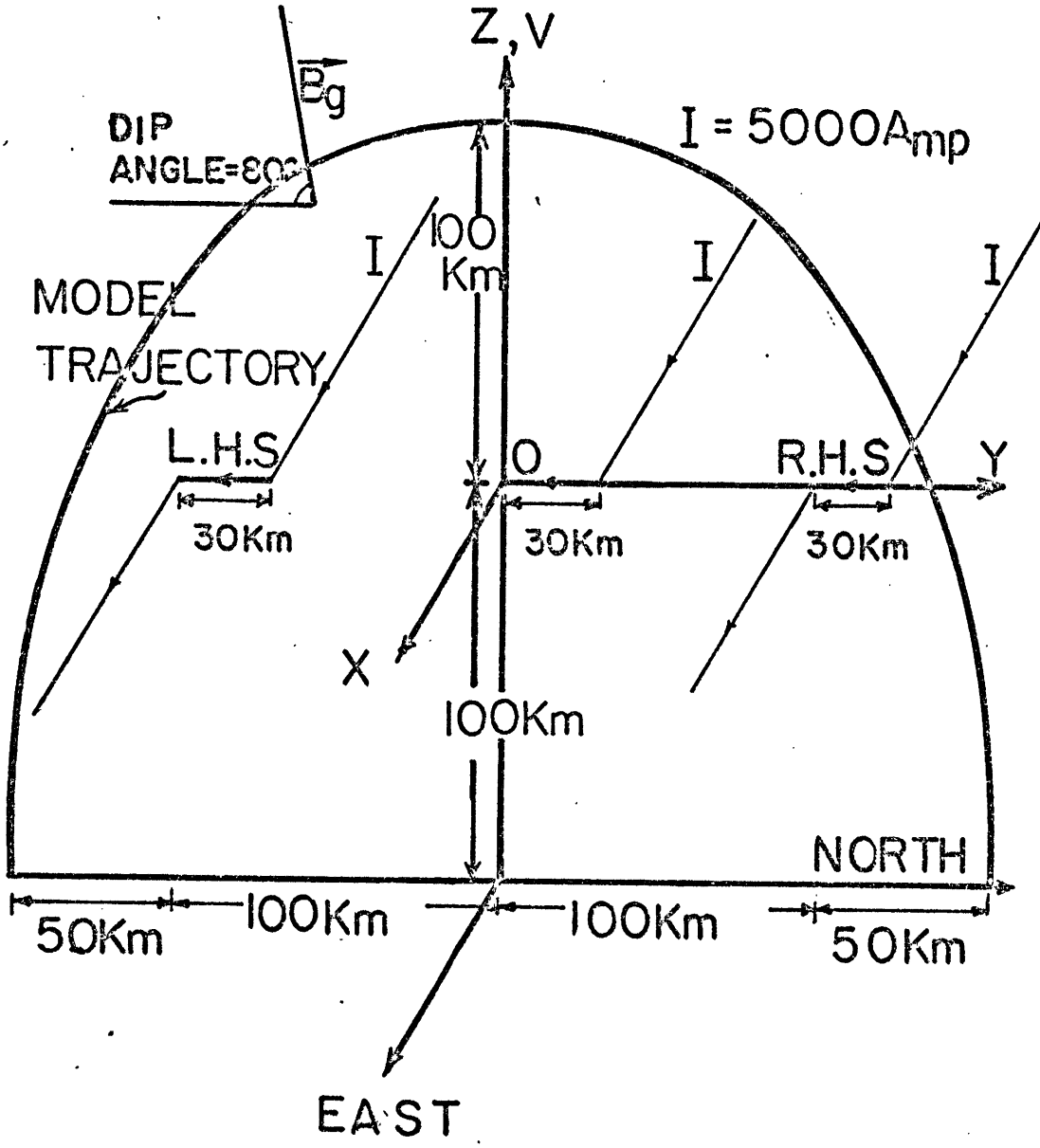
Z, V
$\vec{B}_g$
DIP
ANGLE=80°
I = 5000Amp
100
Km
I
I
I
MODEL
TRAJECTORY
L.H.S
O
R.H.S
Y
30Km
30Km
30Km
X
100Km
NORTH
50Km
100Km
100Km
50Km
EAST

FIGURE 4

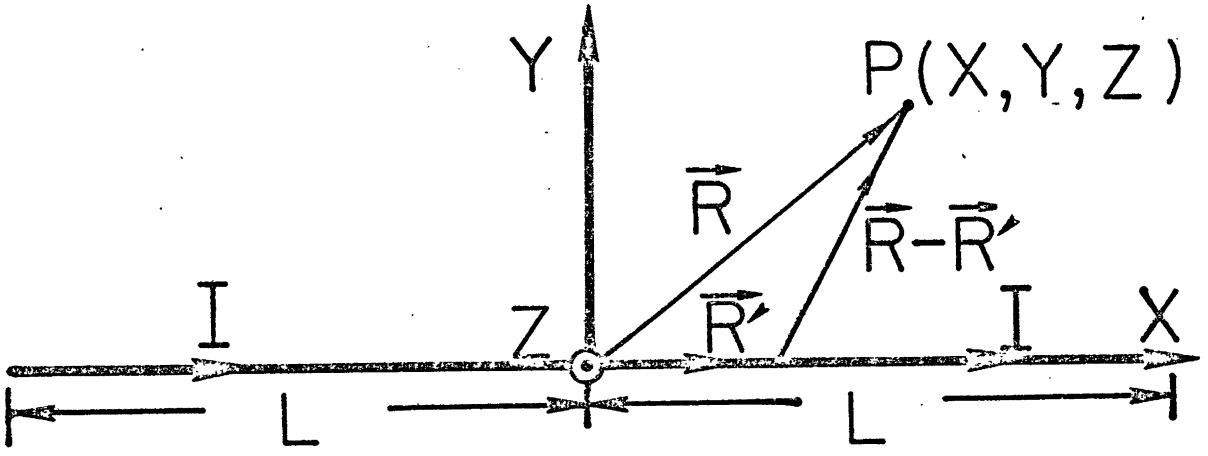

LINE CURRENT

FIGURE 5A

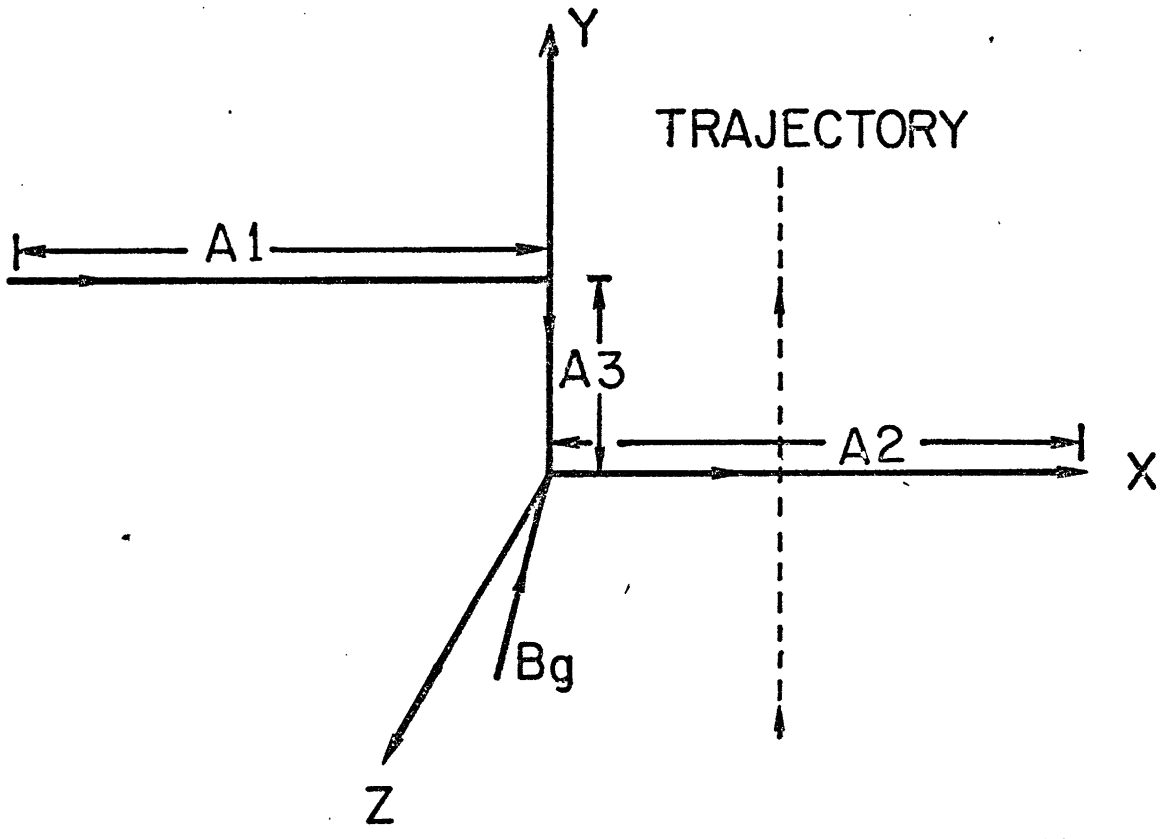

LINE CURRENT

FIGURE 5B

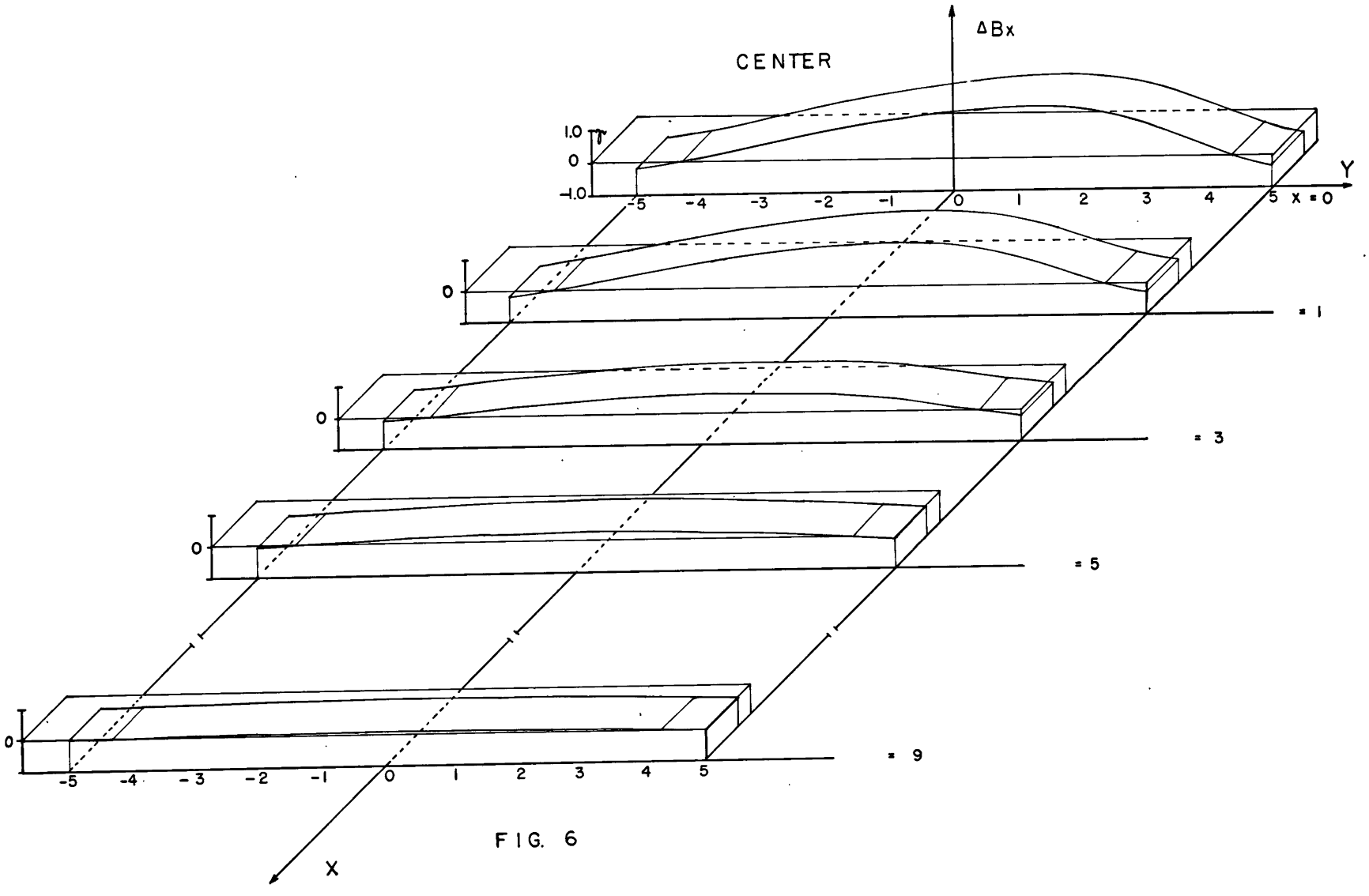

FIG. 6

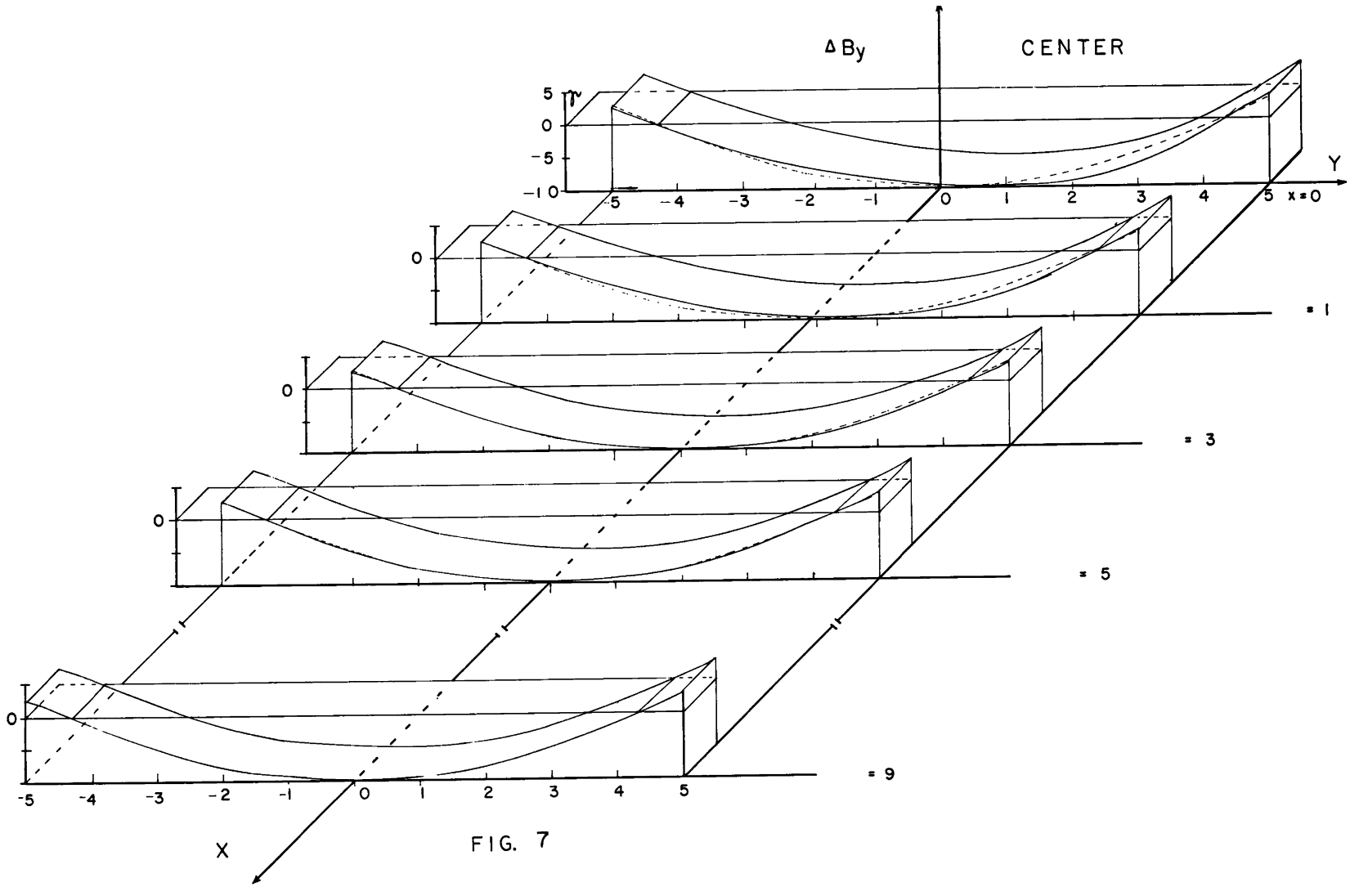

FIG. 7

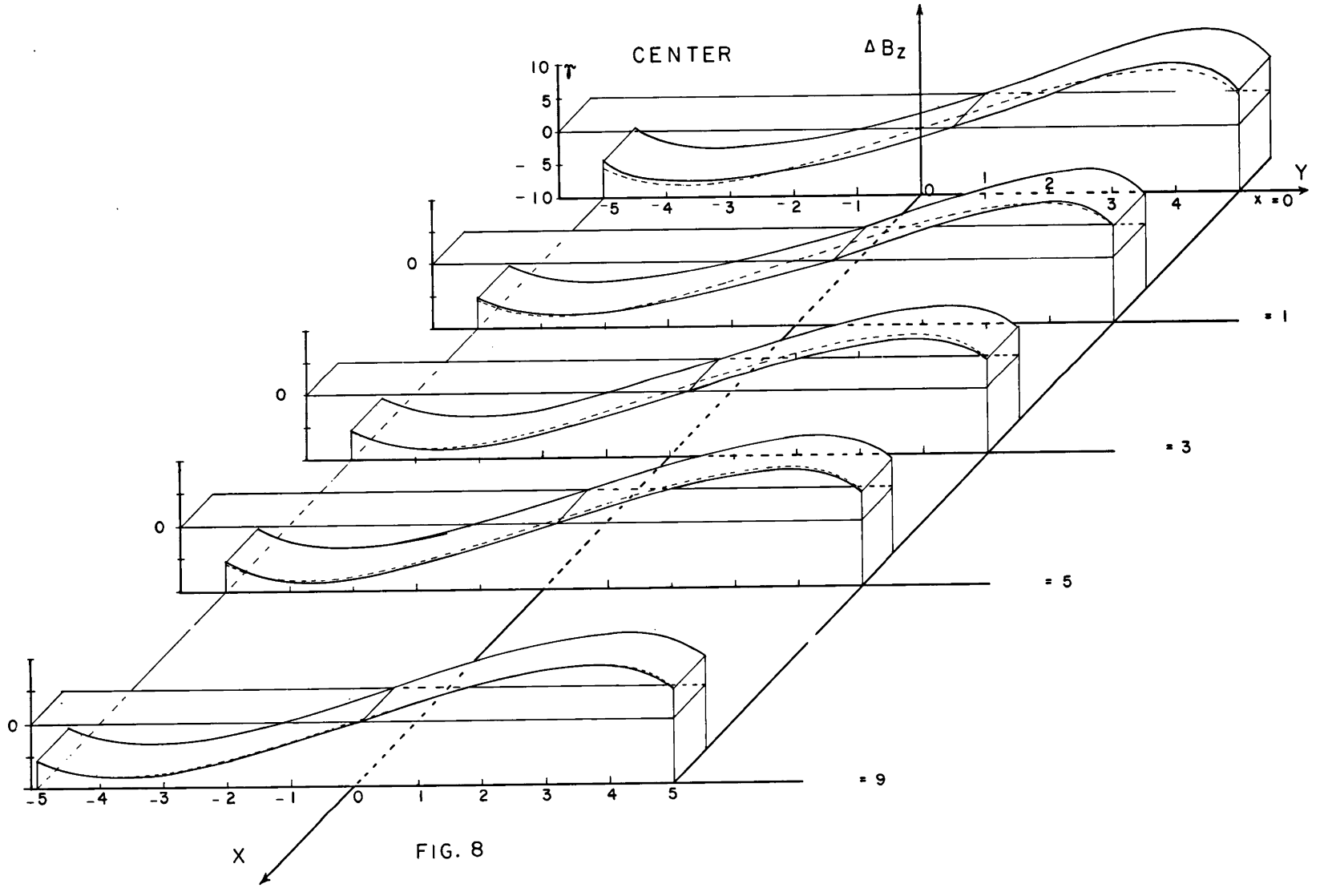

FIG. 8

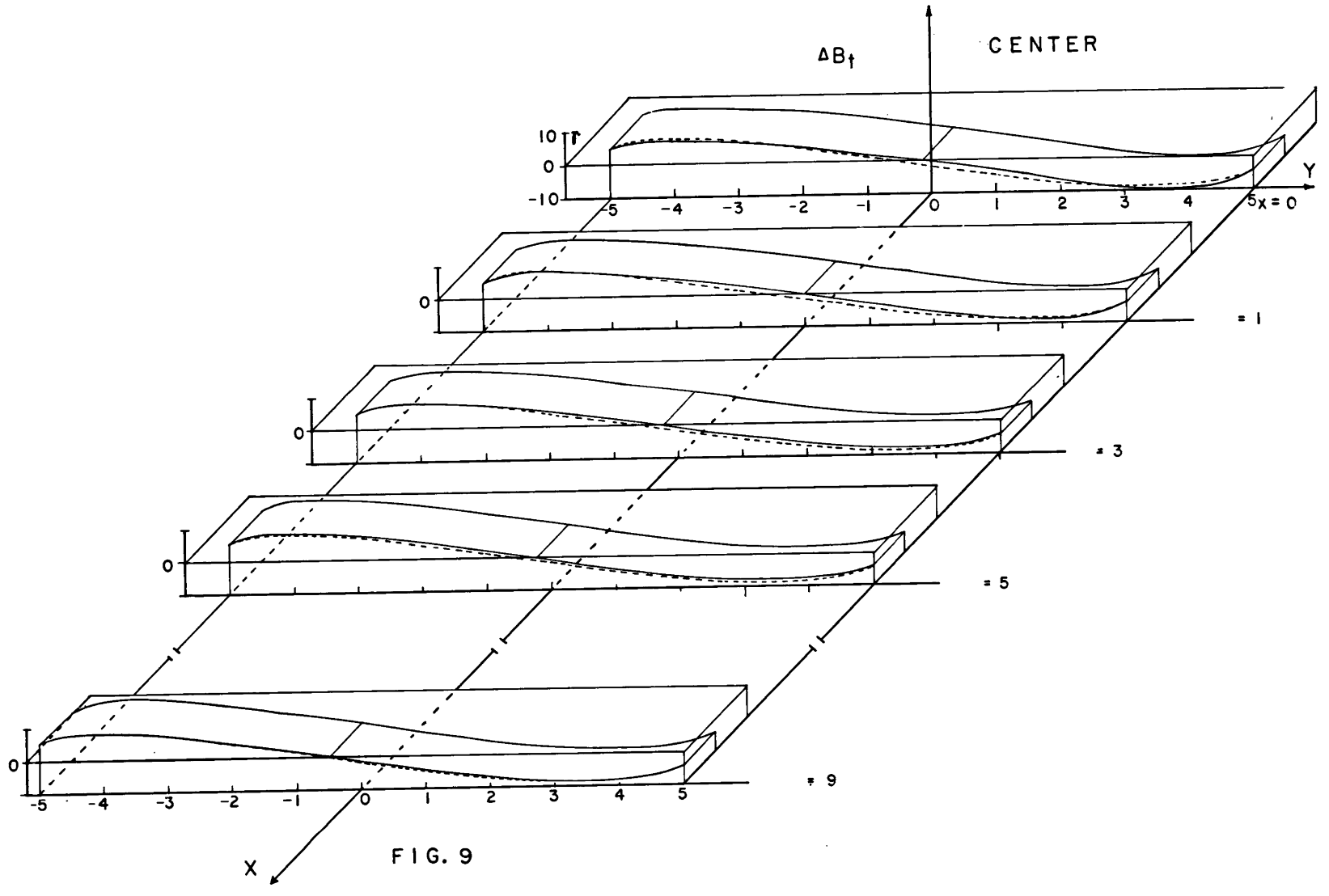

FIG. 9

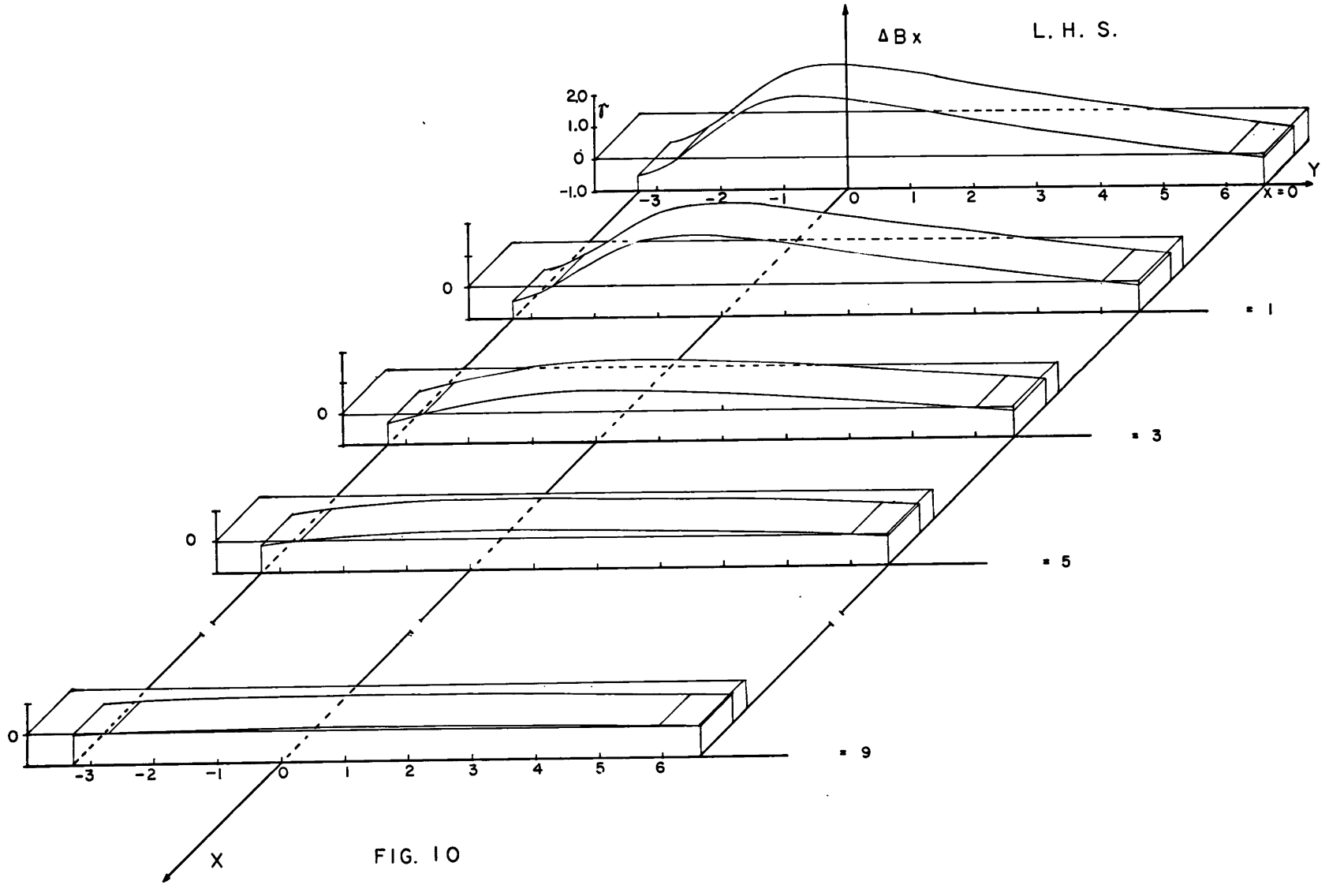

FIG. 10

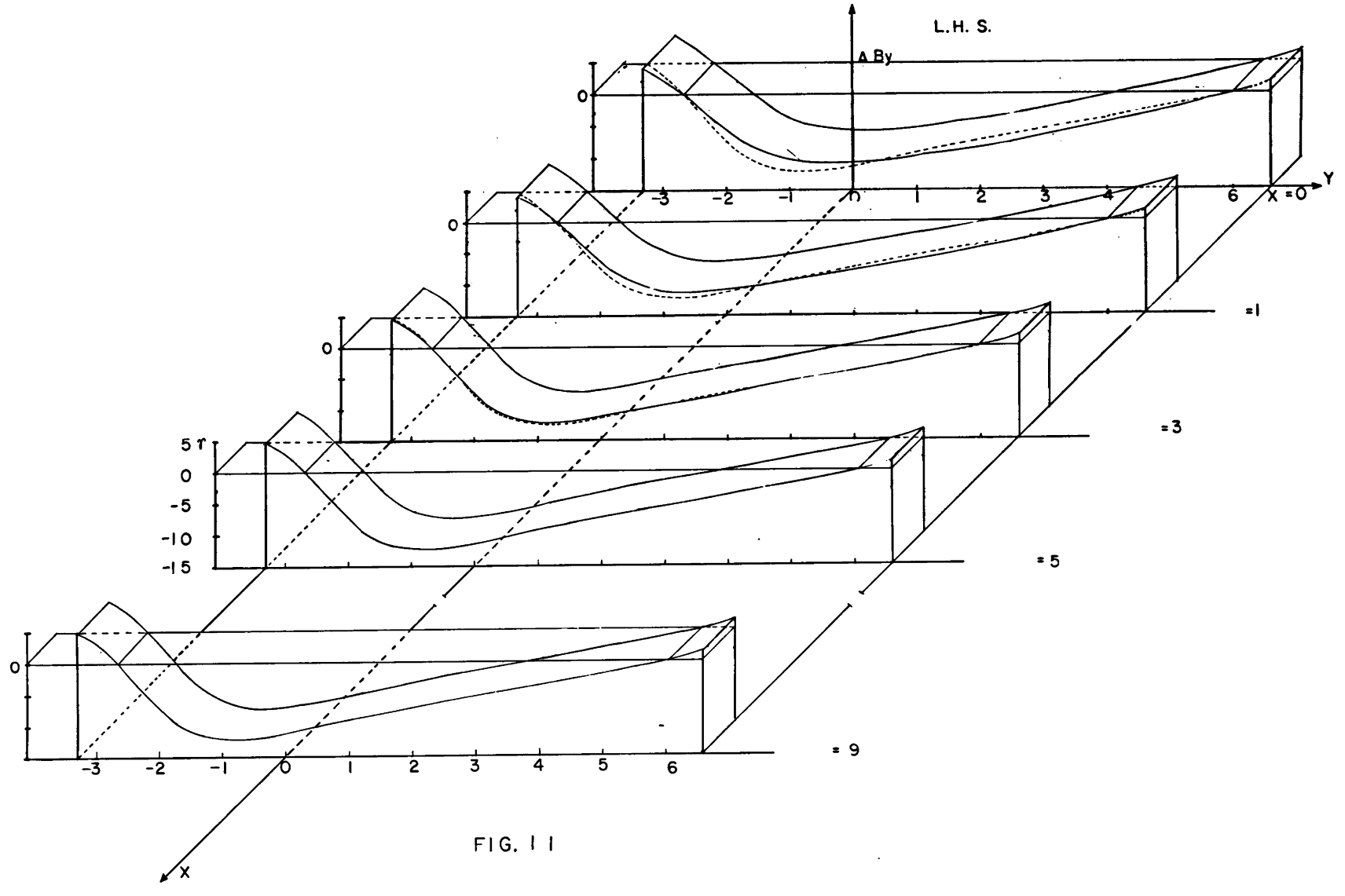

FIG. 11

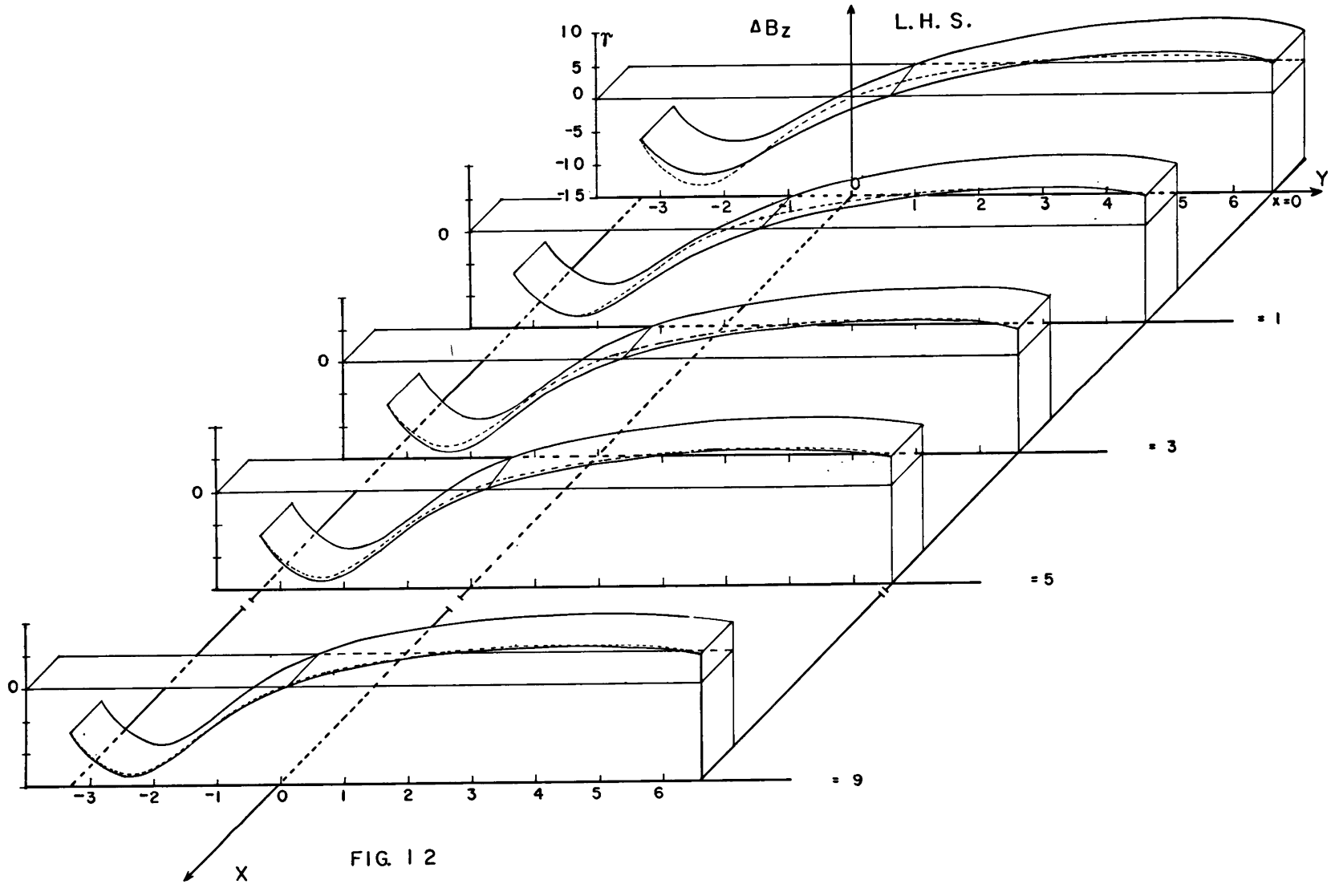

FIG. 12

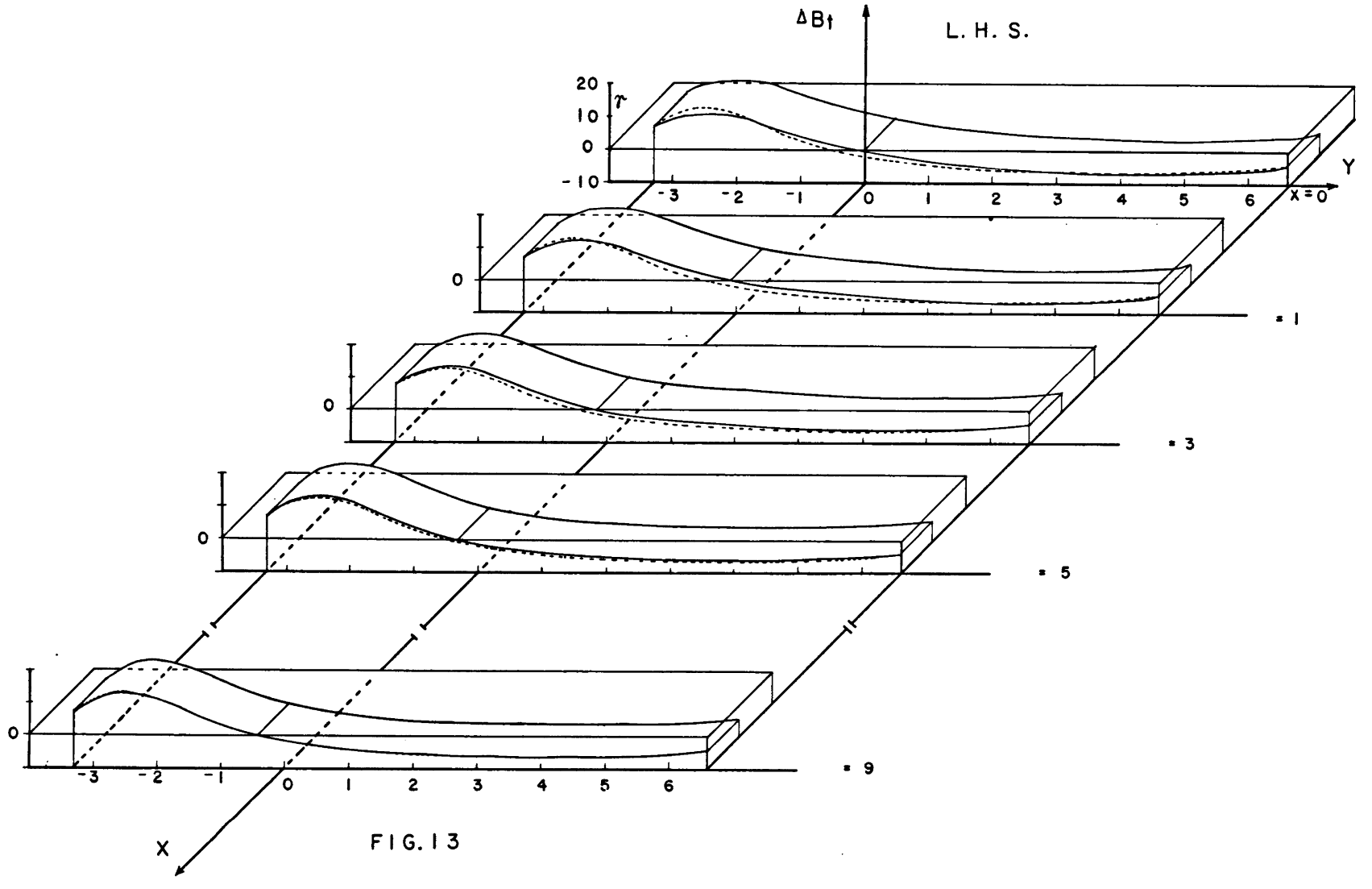

FIG. 13

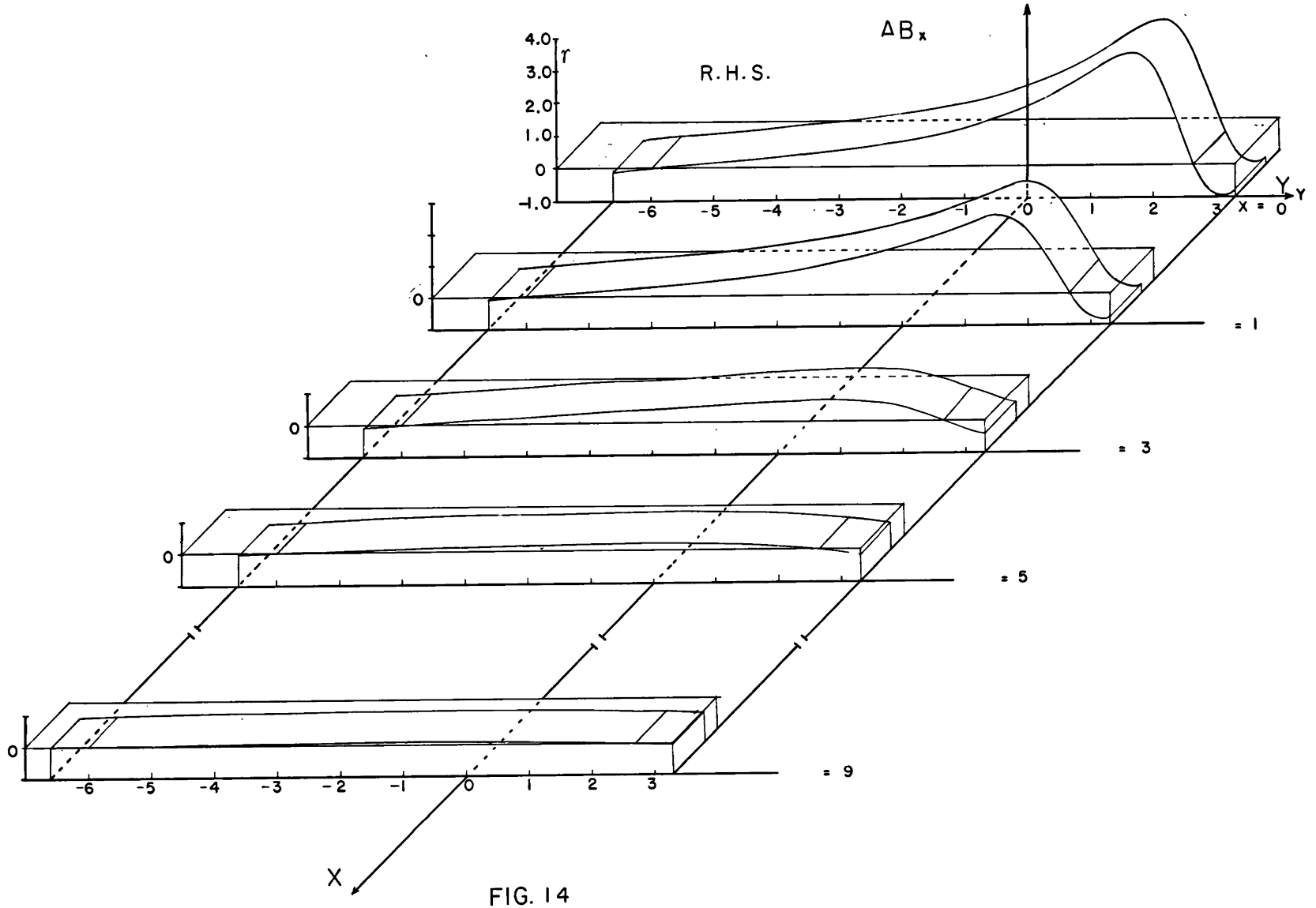

FIG. 14

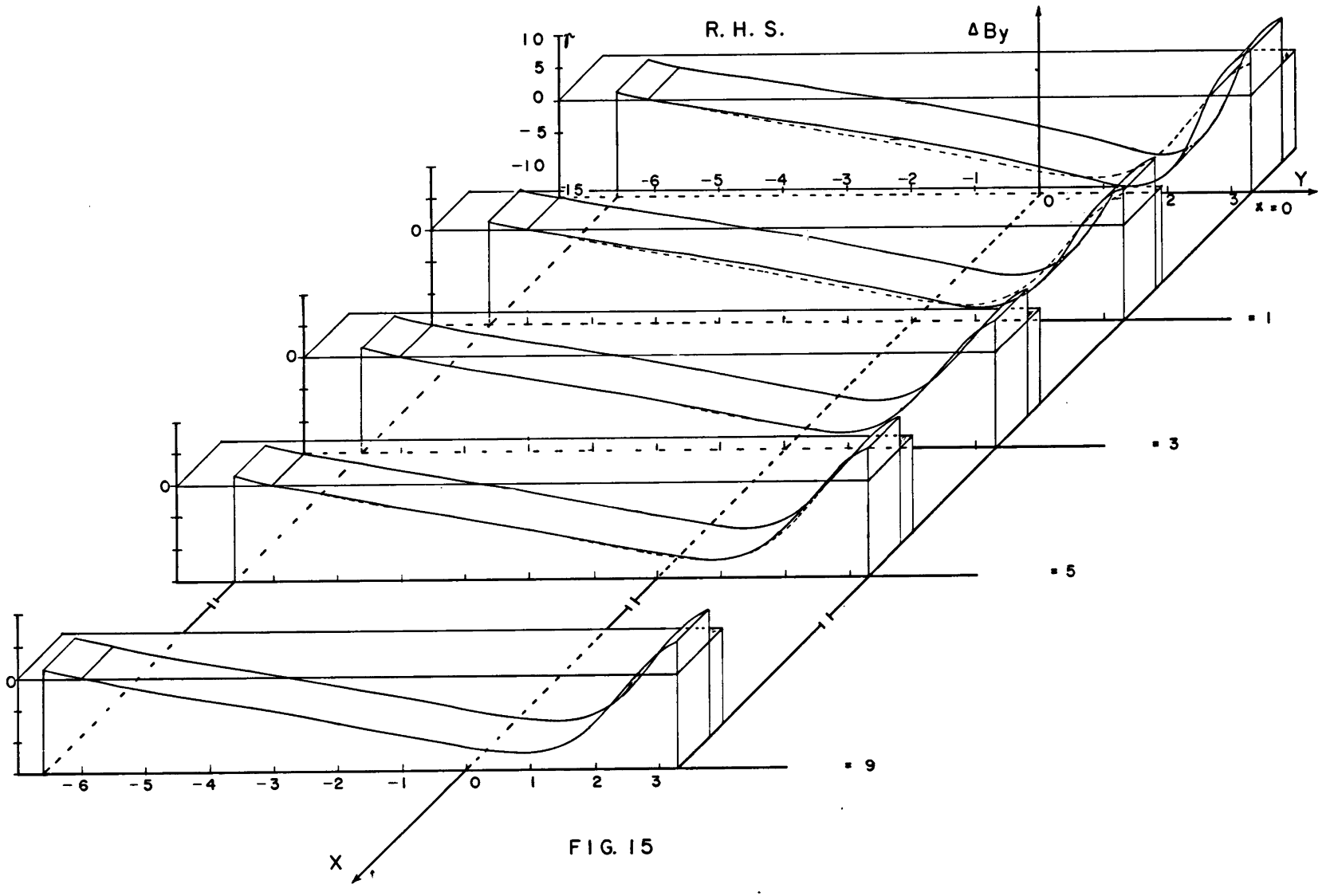

FIG. 15

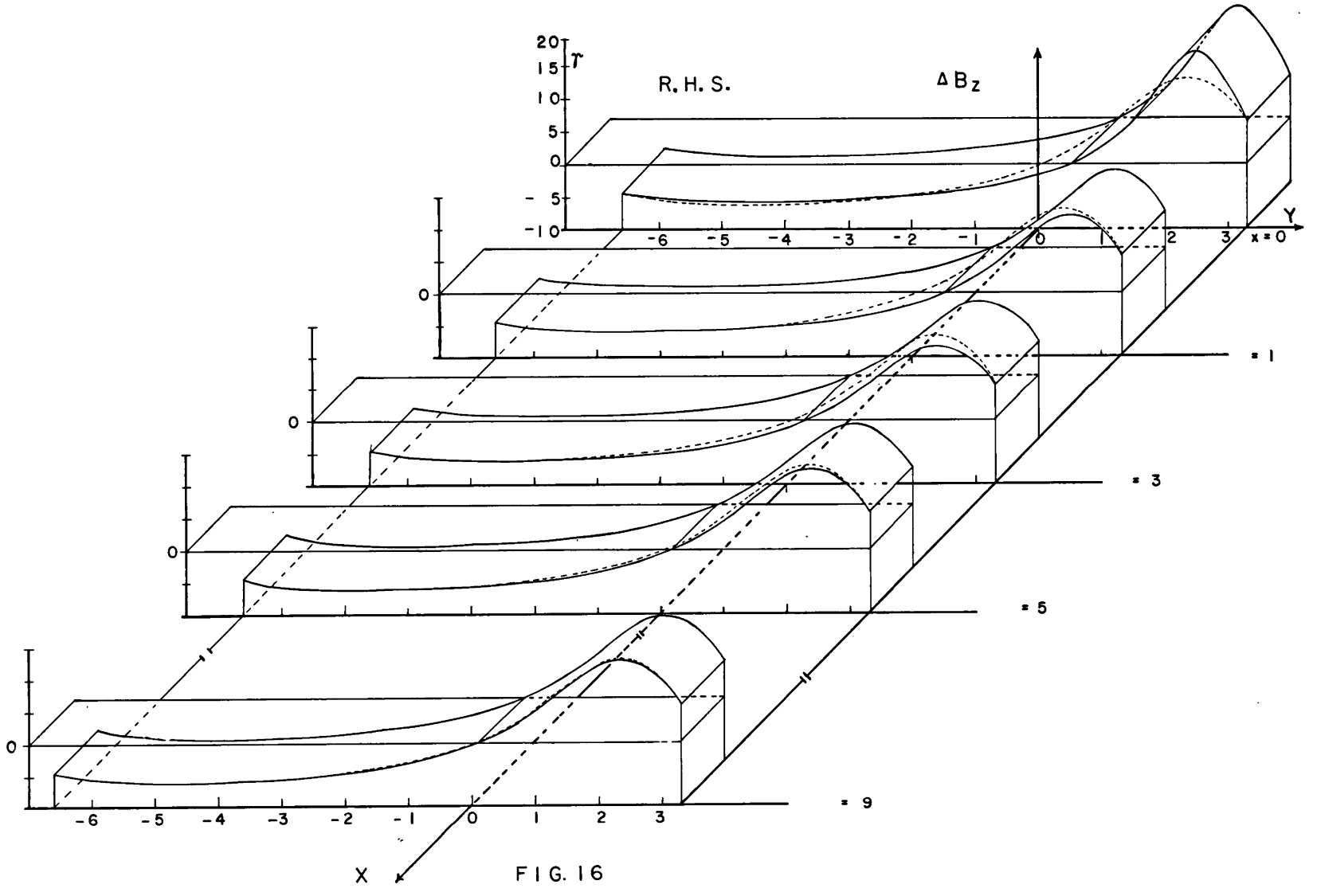

FIG. 16

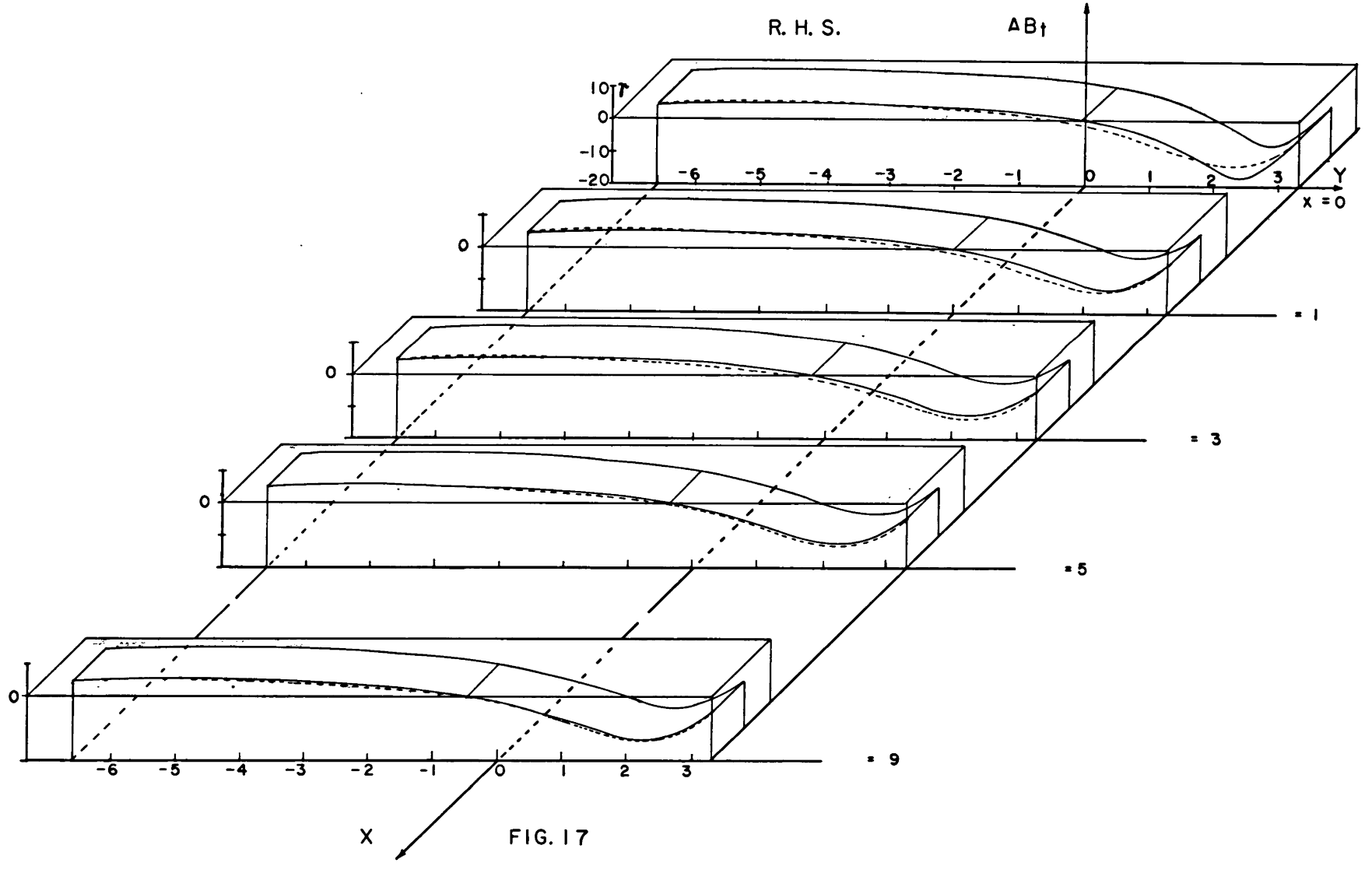

FIG. 17

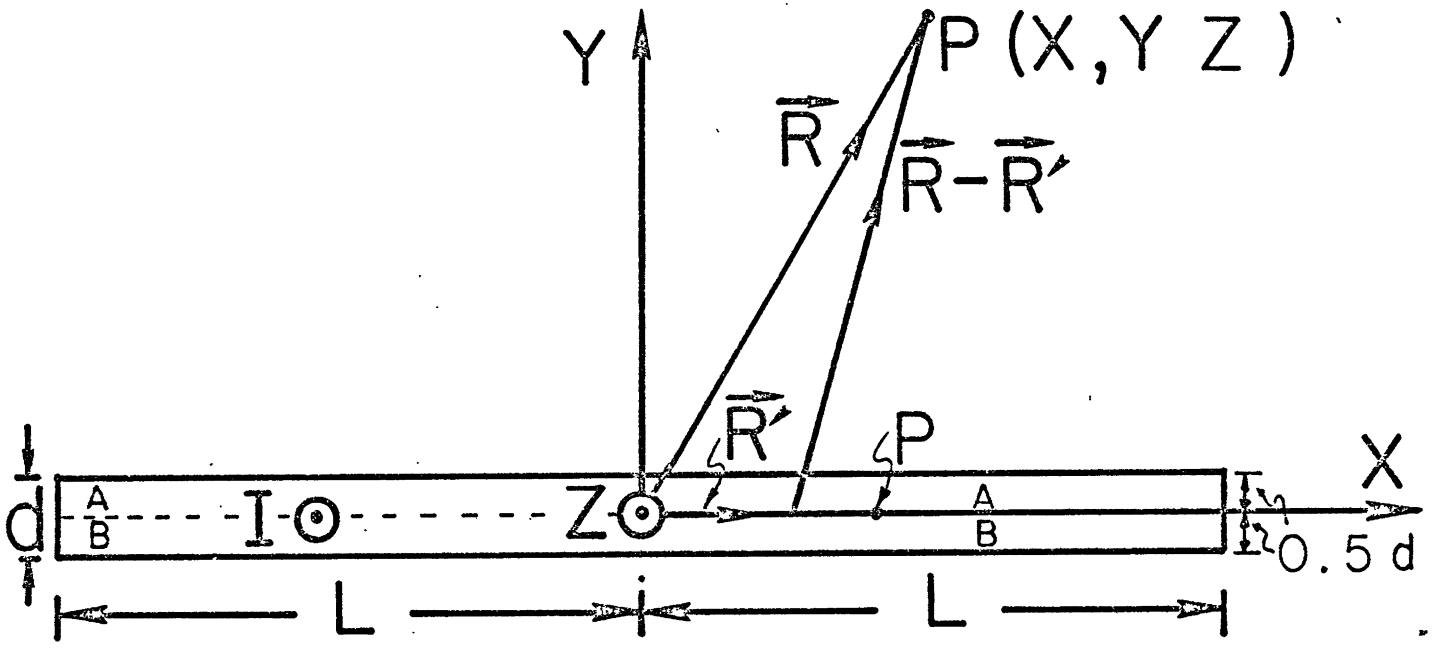

SHEET CURRENT

FIGURE 18A

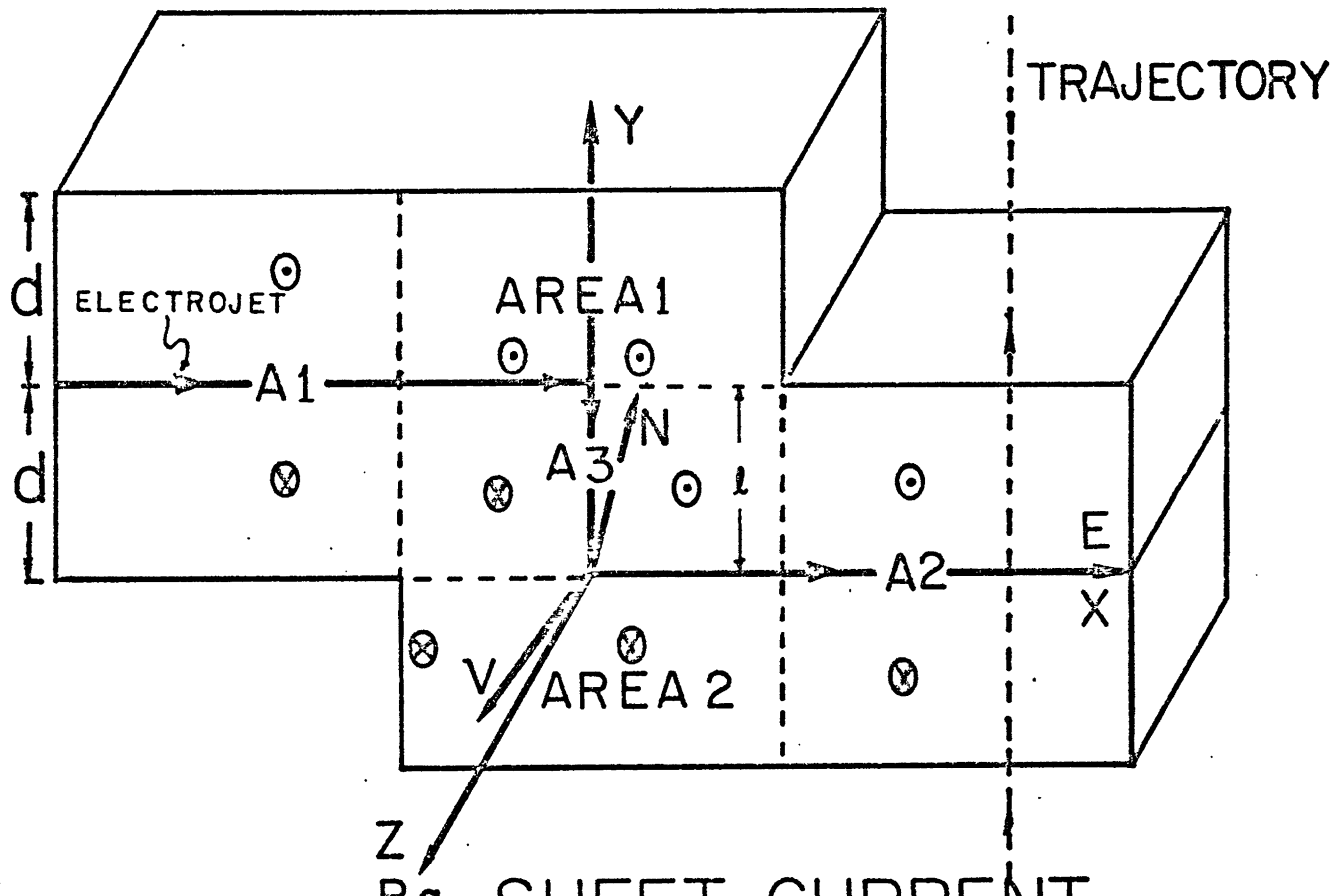
TRAJECTORY
Y
d
ELECTROJET
AREA1
A1
N
A3
d
l
E
A2
X
V
AREA 2
Z
-Bg
SHEET CURRENT

FIGURE 18B

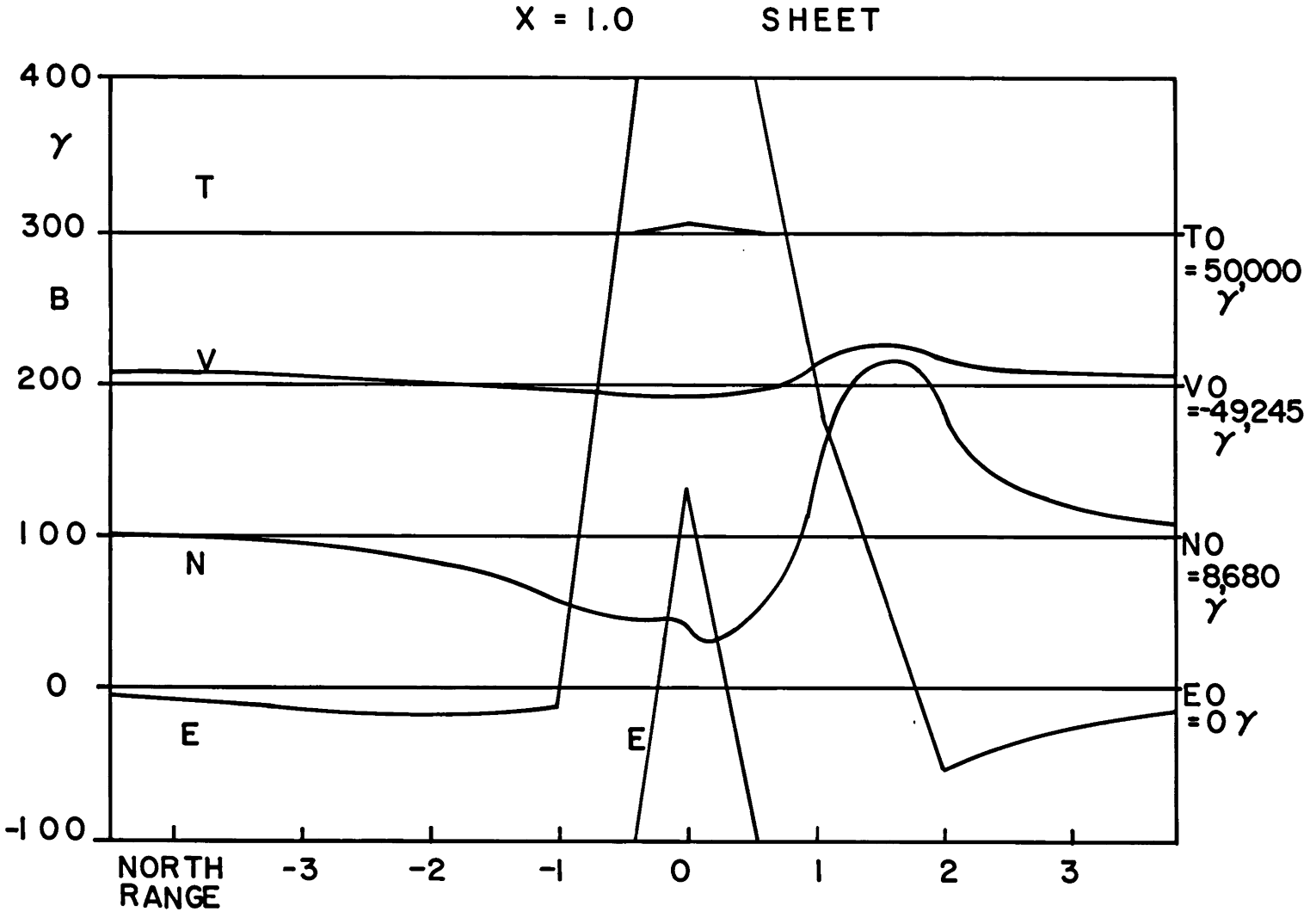
X = 1.0 SHEET
400
γ
300
B
200
100
0
-100
T
V
N
E
E
T0
= 50000
γ'
V0
=-49,245
γ'
N0
=8,680
γ'
E0
=0 γ
NORTH
RANGE
-3
-2
-1
0
1
2
3

FIG. 19

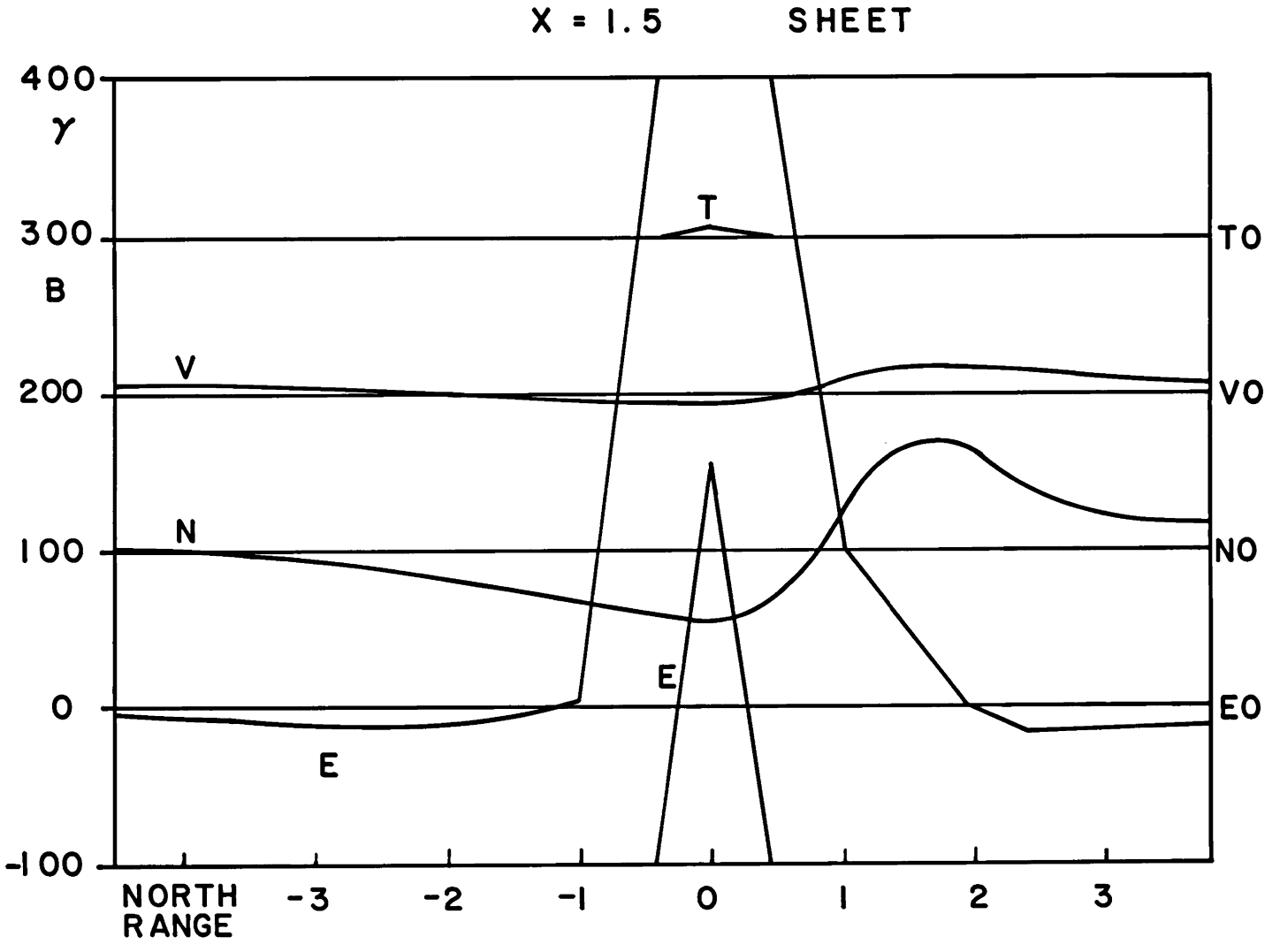
X = 1.5 SHEET
400
γ
300
B
200
100
0
-100
T
V
N
E
E
TO
VO
NO
EO
NORTH
RANGE
-3
-2
-1
0
1
2
3

FIG. 20

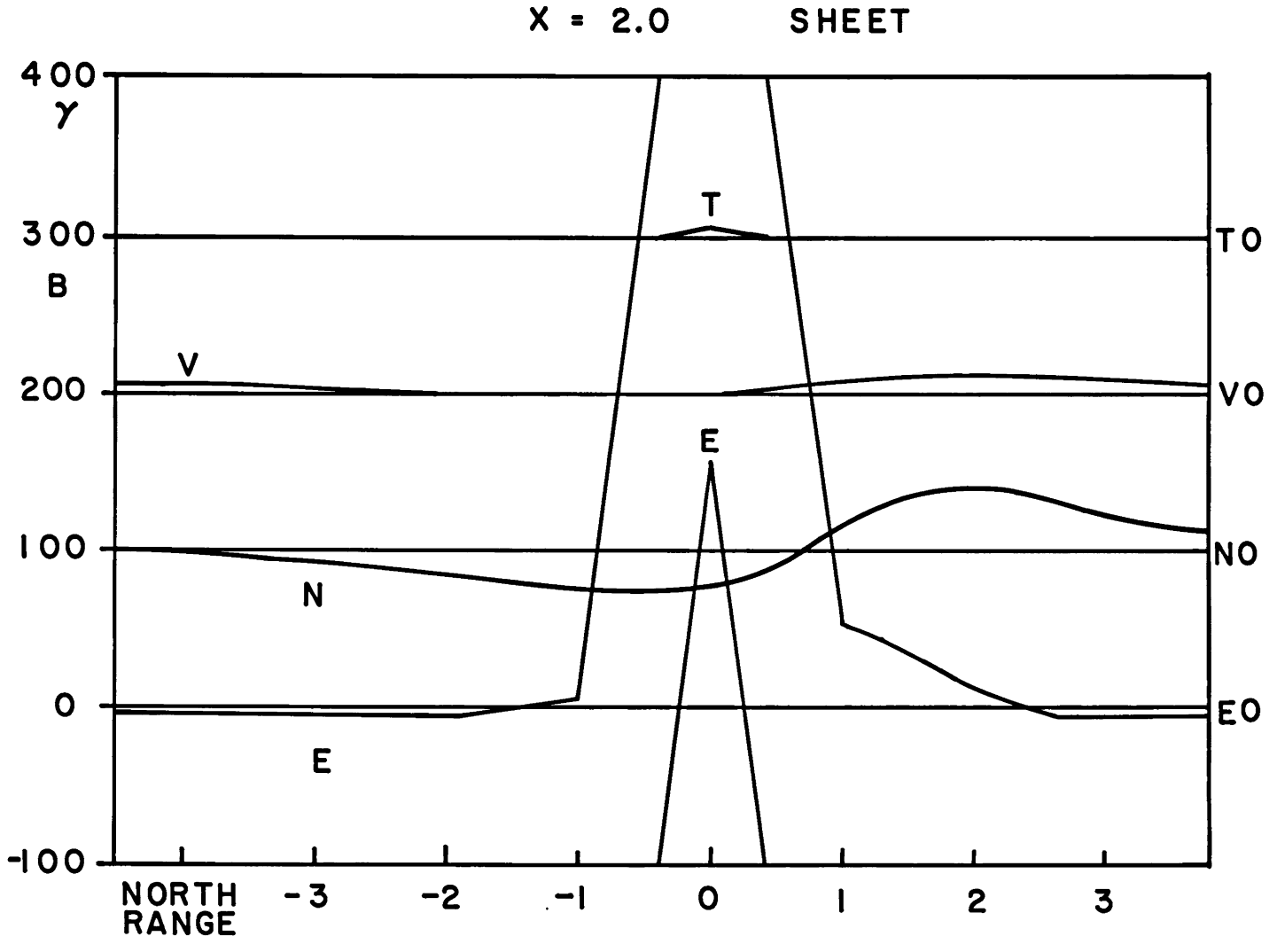
X = 2.0 SHEET
400
γ
300
B
200
100
0
-100
T
V
E
N
E
TO
VO
NO
EO
NORTH
RANGE
-3
-2
-1
0
1
2
3

FIG. 21

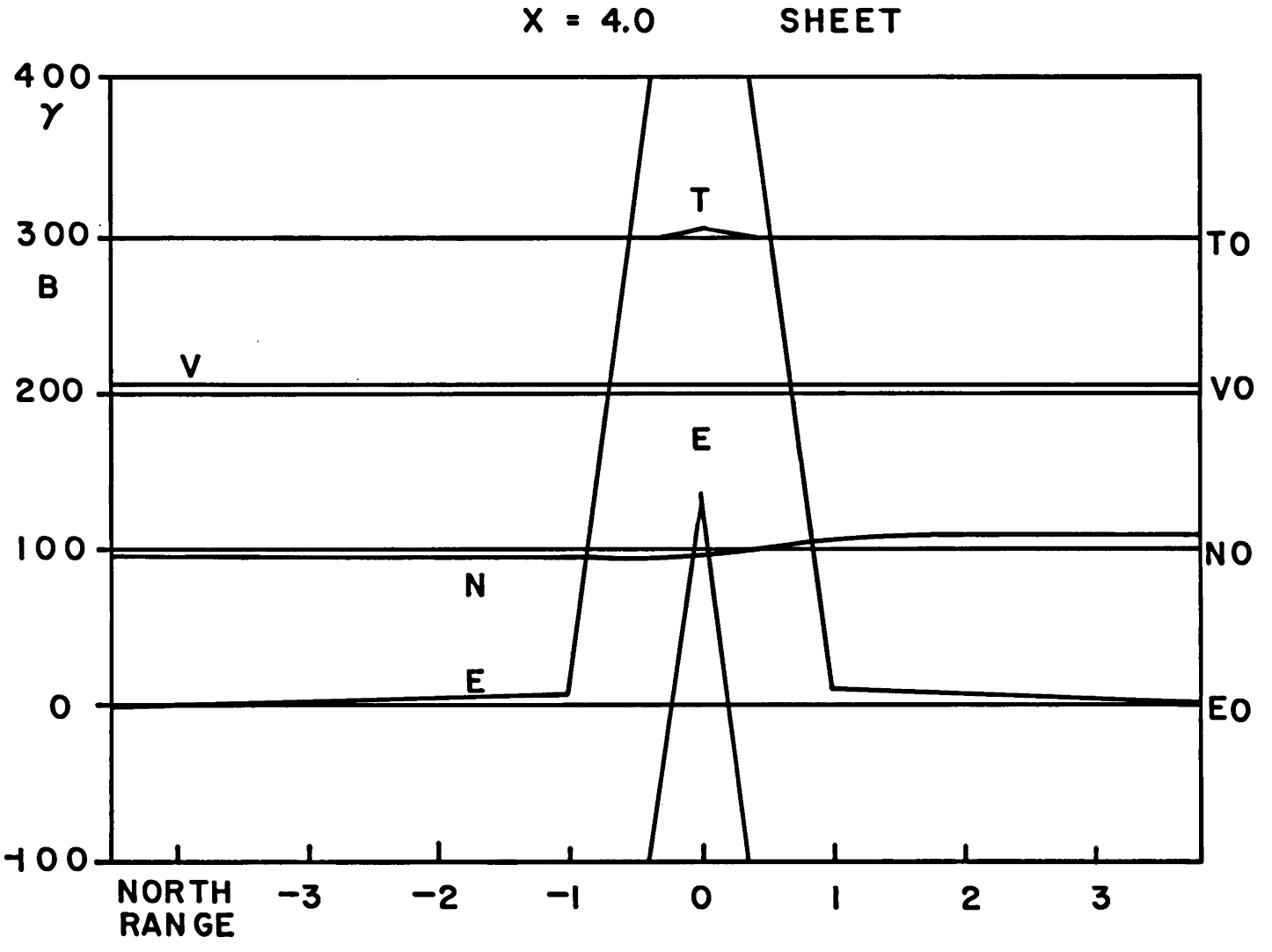
X = 4.0 SHEET
400
γ
300
B
200
100
0
-100
T
TO
V
VO
E
N
NO
E
EO
NORTH
RANGE
-3
-2
-1
0
1
2
3

FIG. 22

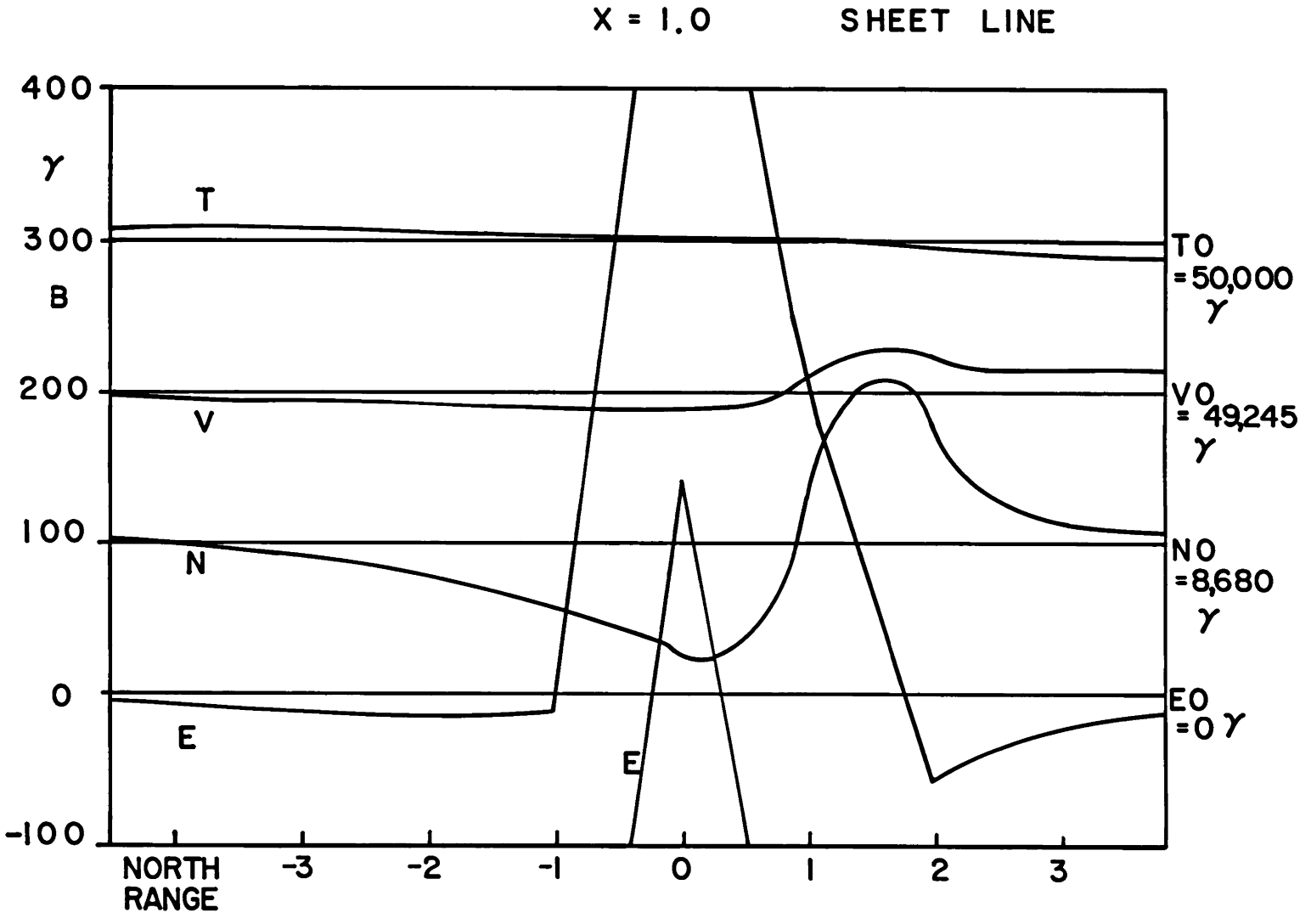
X = 1.0
SHEET LINE
400
γ
300
B
200
100
0
-100
T
V
N
E
E
TO
=50,000
γ
VO
= 49,245
γ
NO
=8,680
γ
EO
=0 γ
NORTH
RANGE
-3
-2
-1
0
1
2
3

FIG. 23

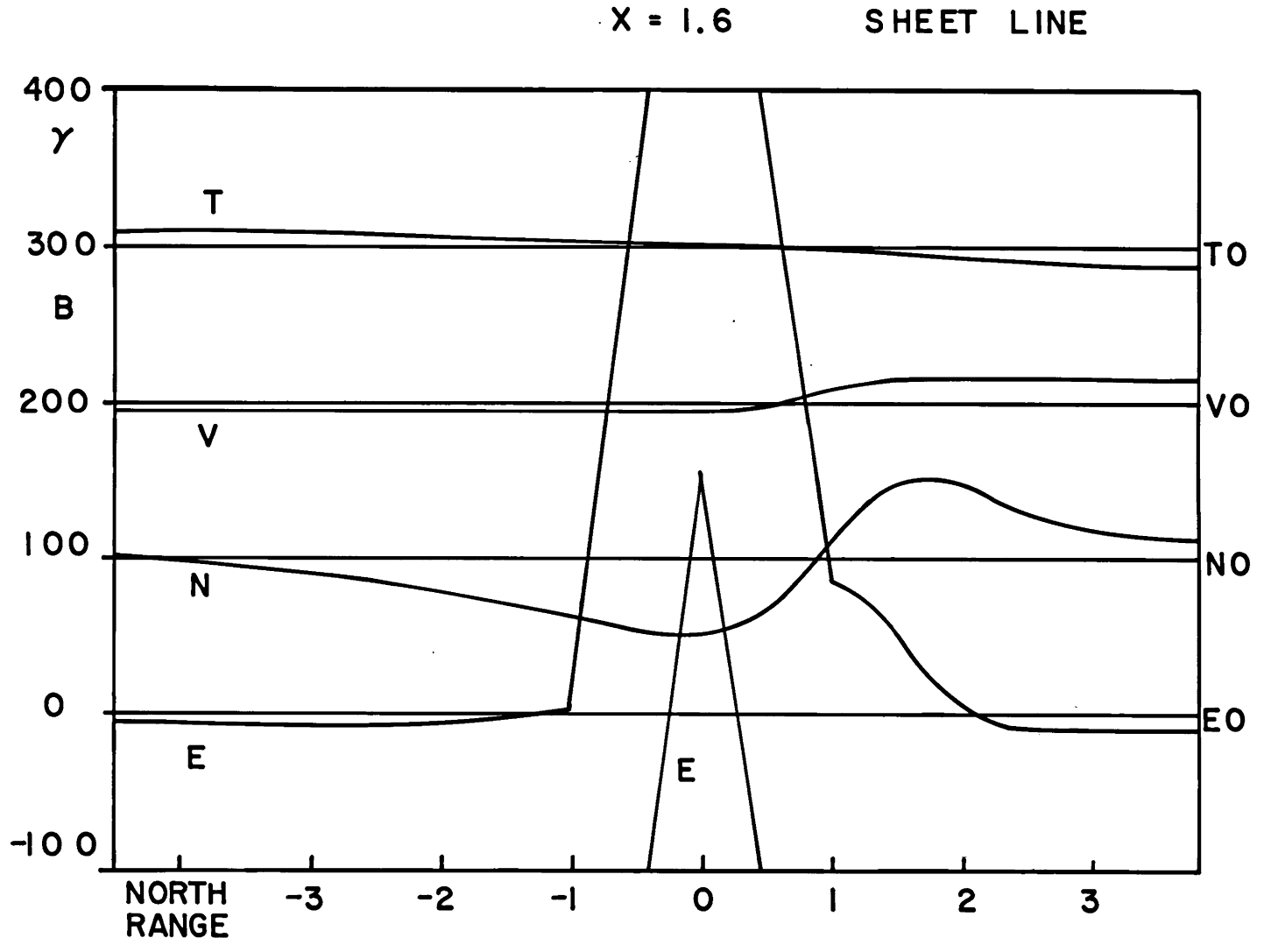
X = 1.6
SHEET LINE
400
γ
300
200
100
0
-100
T
B
V
N
E
E
TO
VO
NO
EO
NORTH
RANGE
-3
-2
-1
0
1
2
3

FIG. 24

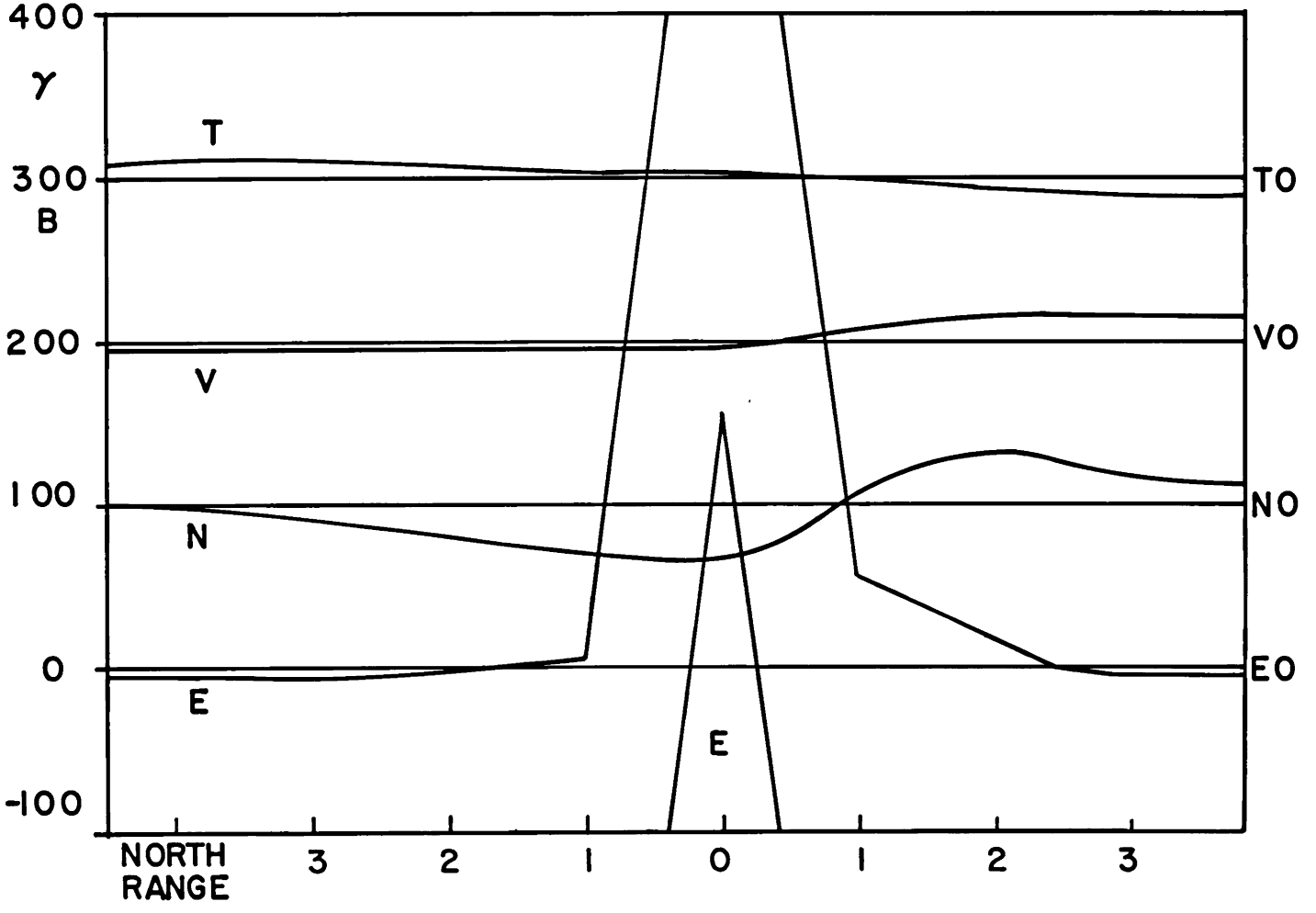
X = 2.0 SHEET LINE
400
γ
300
B
200
100
0
-100
T
TO
V
VO
N
NO
E
EO
E
NORTH
RANGE
3
2
1
0
1
2
3

FIG. 25

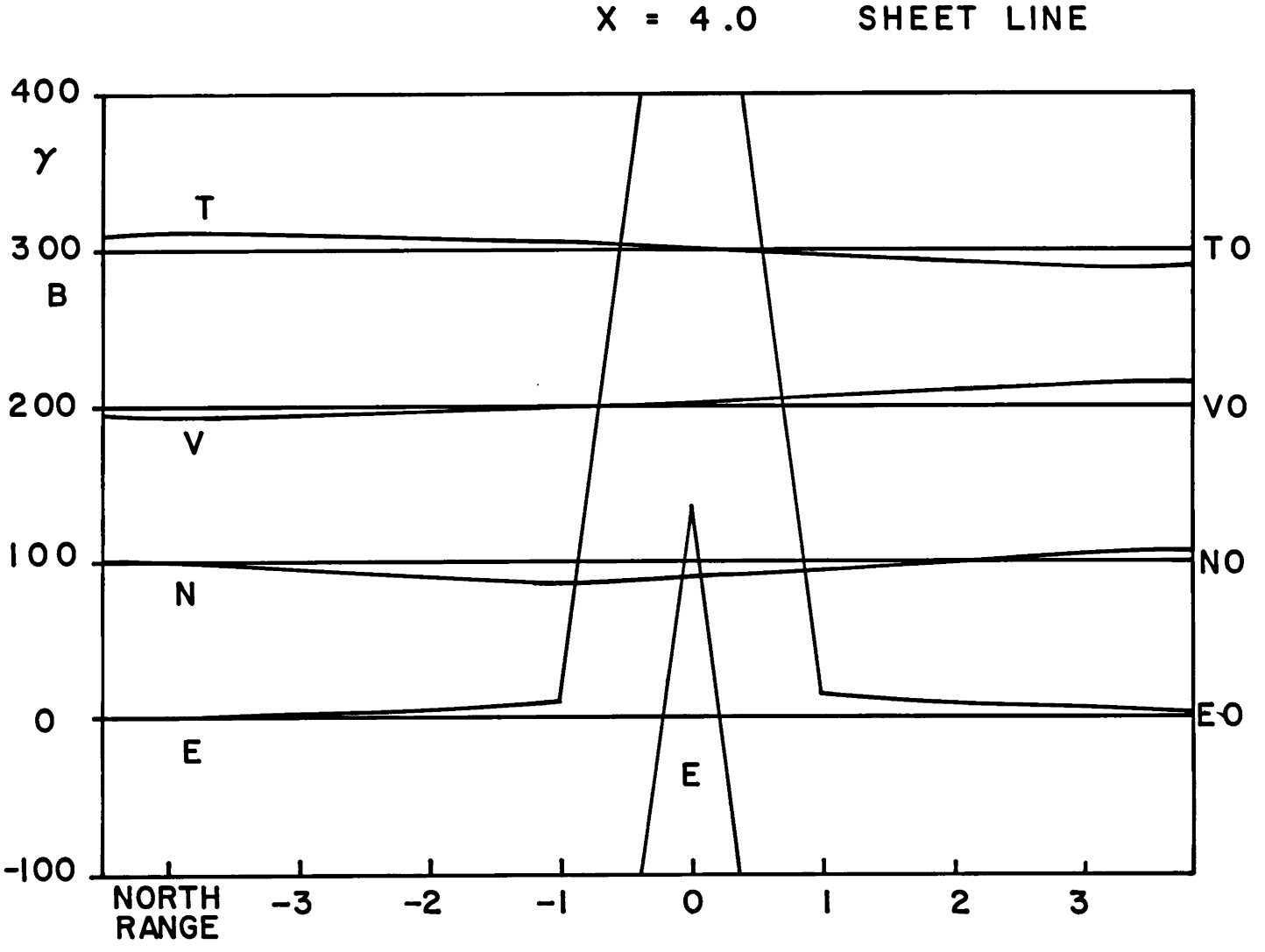
X = 4.0 SHEET LINE
400
γ
300
B
200
100
0
-100
T
V
N
E
E
TO
VO
NO
EO
NORTH
RANGE
-3
-2
-1
0
1
2
3

FIG. 26

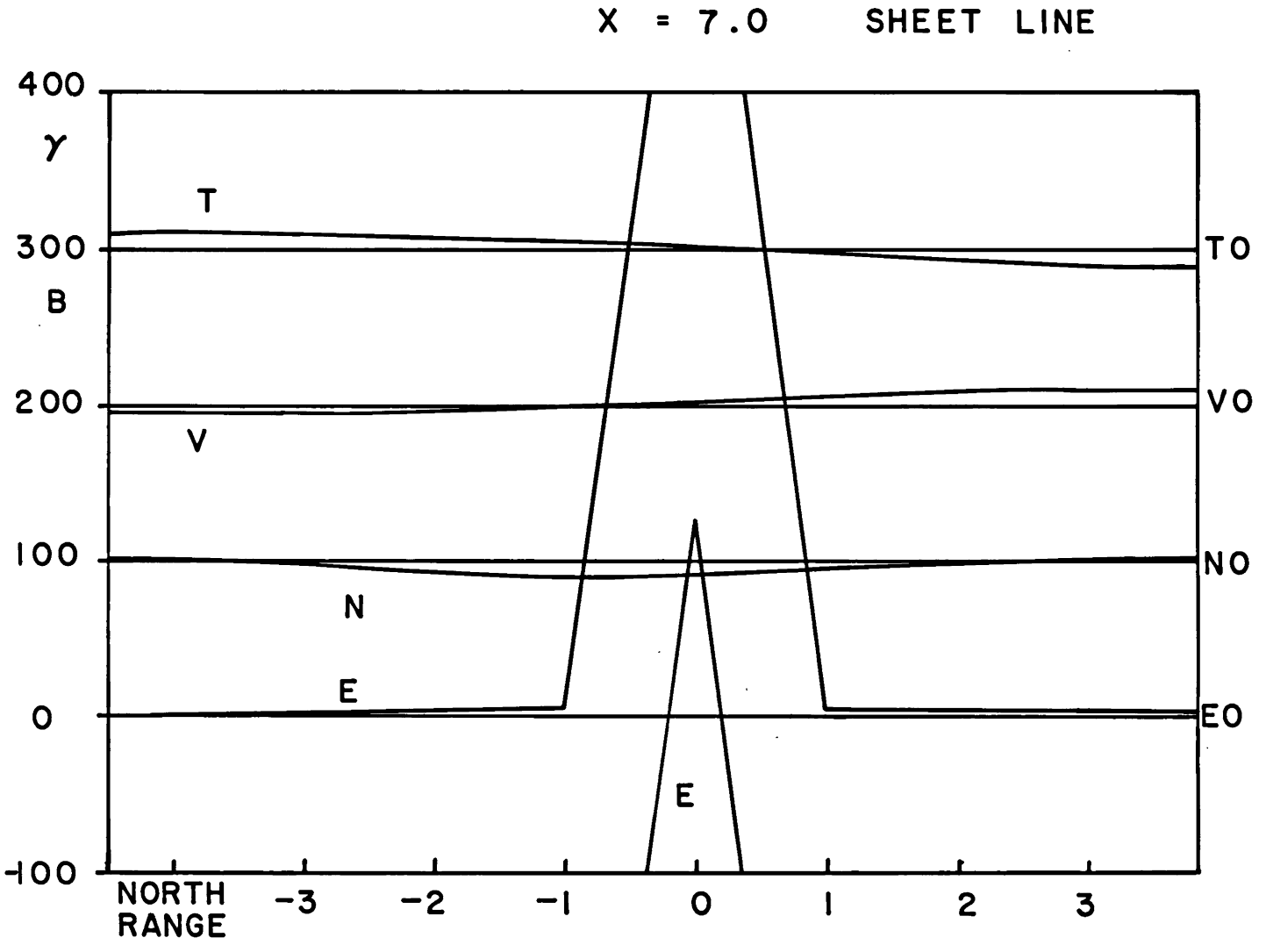
X = 7.0 SHEET LINE
400
γ
300
B
200
100
0
-100
T
V
N
E
E
TO
VO
NO
EO
NORTH
RANGE
-3
-2
-1
0
1
2
3

FIG. 27

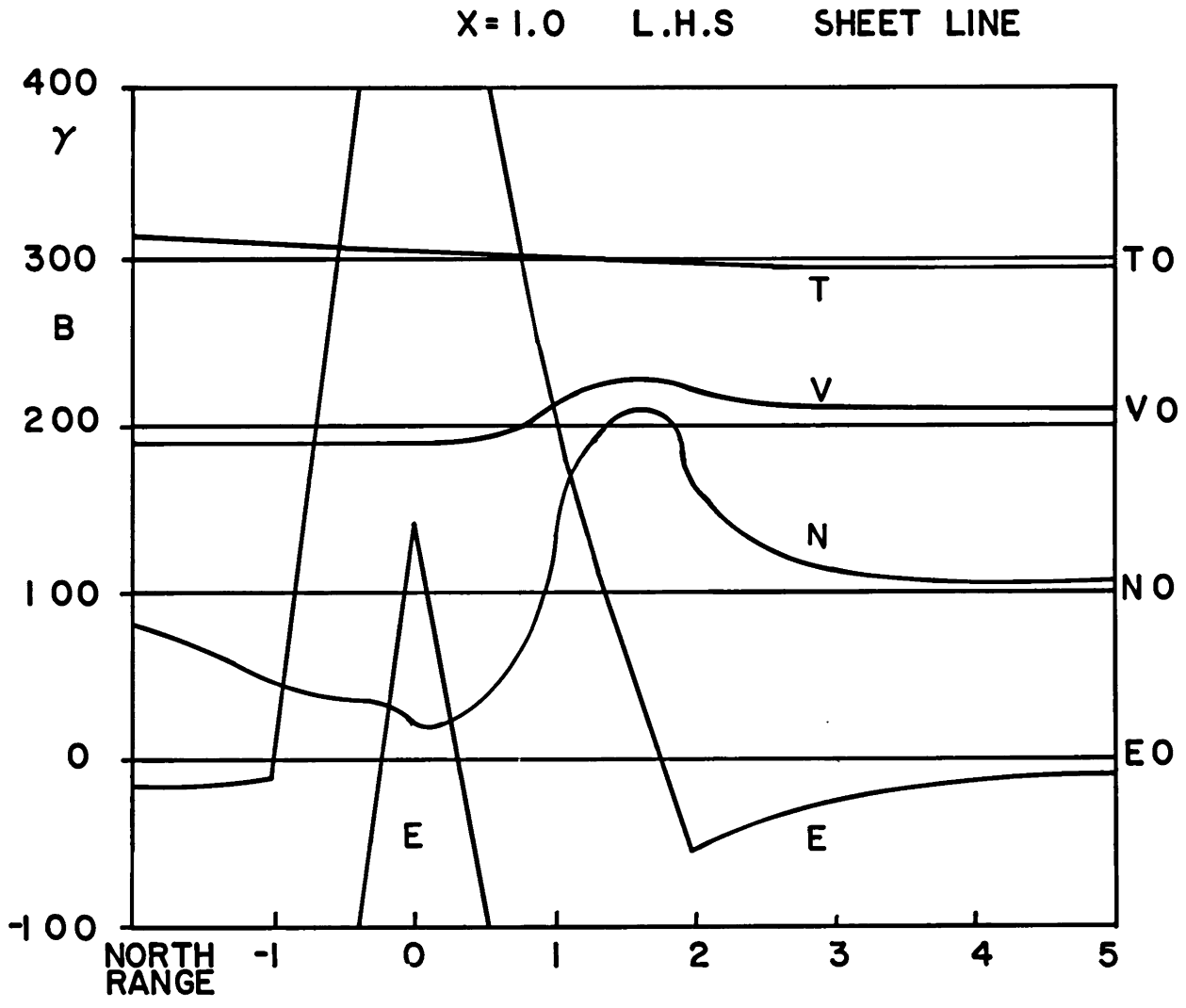
X= 1.0 L.H.S SHEET LINE
400
γ
300
B
200
100
0
-100
T
V
N
E
E
TO
VO
NO
EO
NORTH
RANGE
-1
0
1
2
3
4
5

FIG. 28

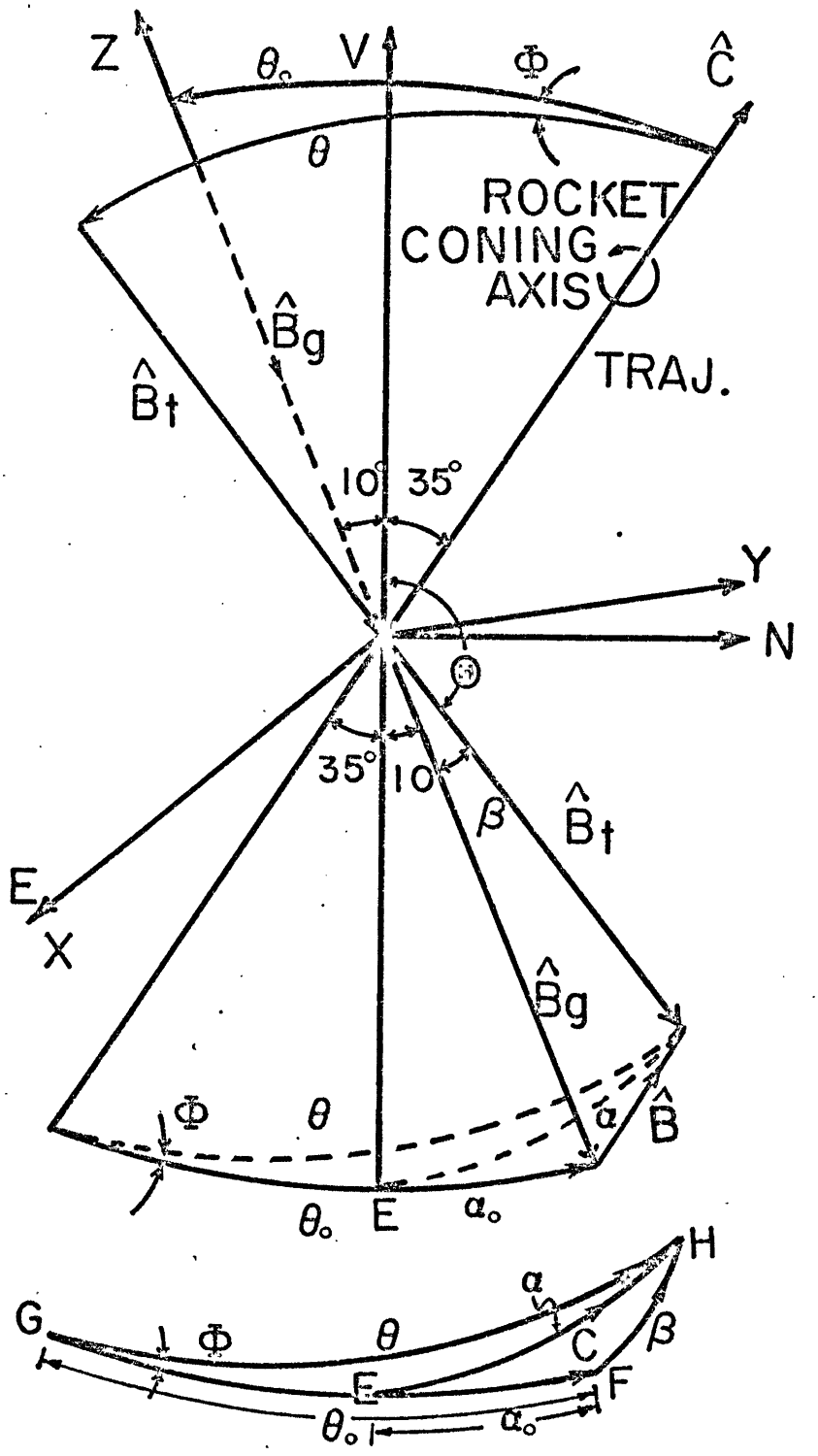
Z
θ₀
V
Φ
Ĉ
θ
ROCKET
CONING
AXIS
TRAJ.
B̂g
B̂t
10°
35°
Y
N
35°
10°
β
B̂t
E
X
B̂g
Φ
θ
α
B̂
θ₀
E
α₀
H
α
G
Φ
θ
C
β
E
F
θ₀
α₀

FIGURE 29

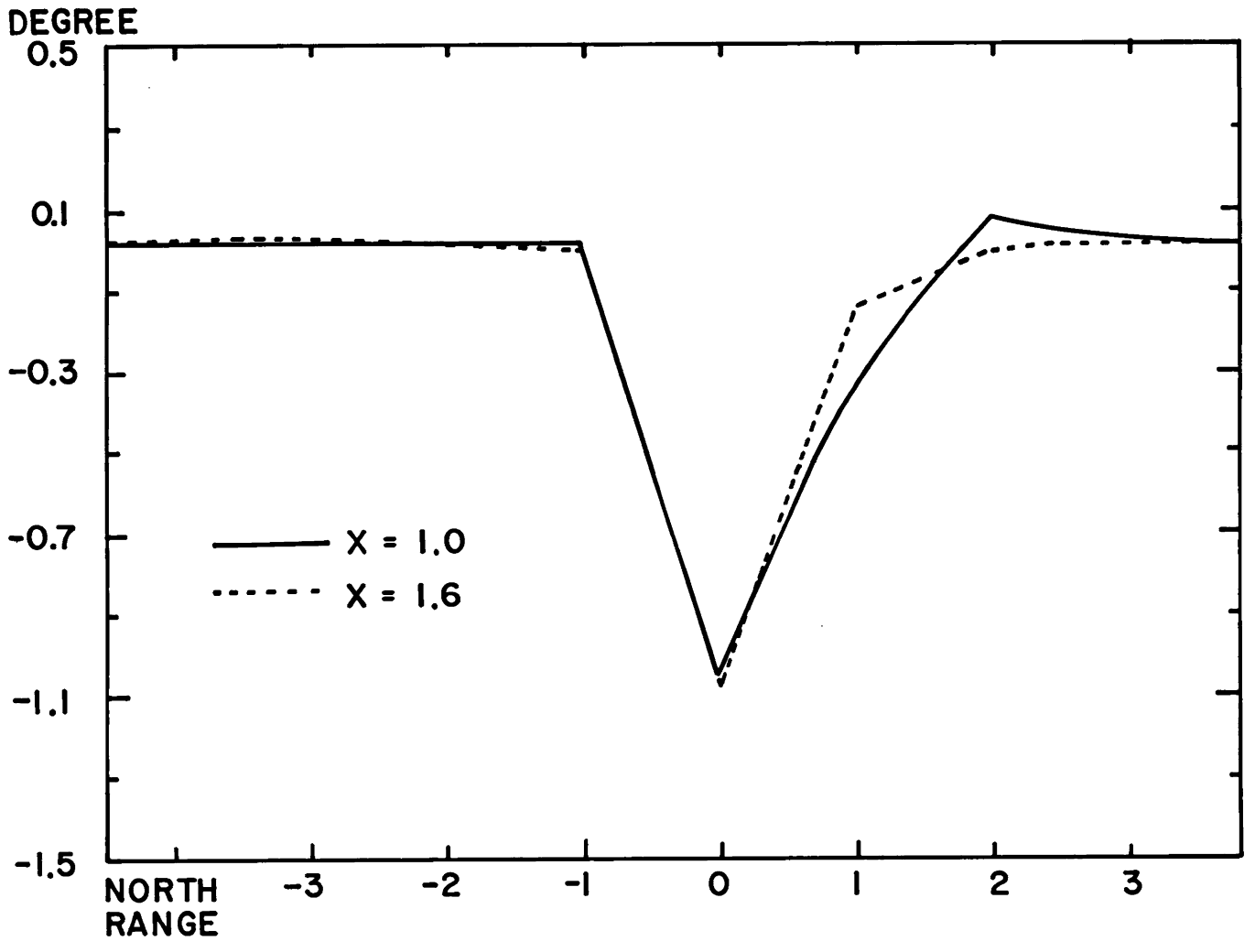

FIG. 30

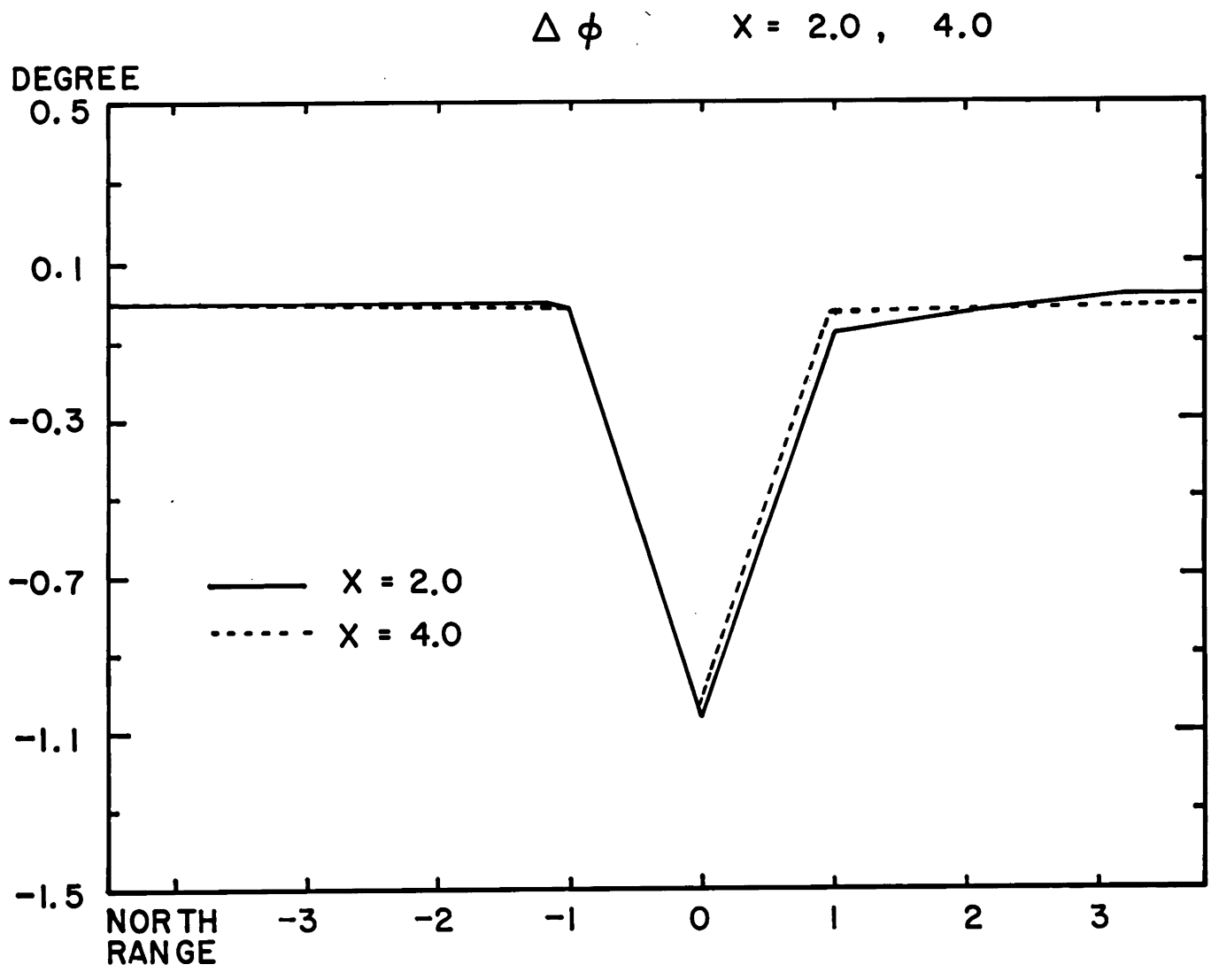

FIG. 31

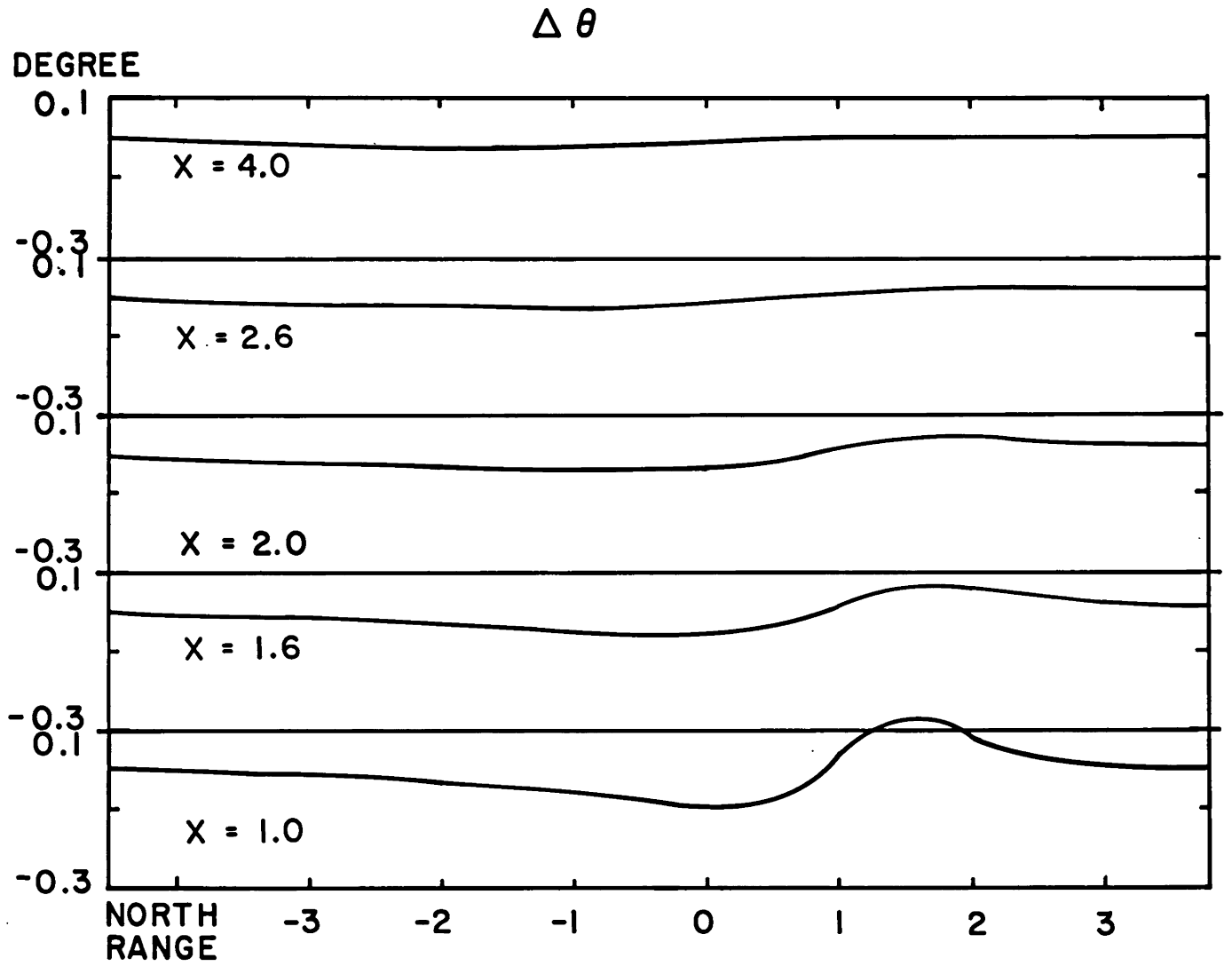
Δ θ
DEGREE
0.1
X = 4.0
-0.3
0.1
X = 2.6
-0.3
0.1
X = 2.0
-0.3
0.1
X = 1.6
-0.3
0.1
X = 1.0
-0.3
NORTH RANGE
-3
-2
-1
0
1
2
3

FIG. 32

FIG. 33 Trajectories

ACKNOWLEDGEMENTS

It is my great pleasure to express my gratitude to my thesis advisor, Dr. Paul A. Cloutier for support and advice during all the phases of this work. I also like to thank Dr. W.J. Burke, Dr. B. R. Sandel and Dr. R. J. Park for many illuminating discussions.

A great deal of encouragement which has been given by Mr. J. Sesiano and Mr. R. Casserly is sincerly appreciated.

This research work was supported by the National Science Coucil, Republic of China, NASA Contract No. NSR-44-006-023 and NASA Contract No. NGL-44-006-012.

REFERENCES

Alfven,H., A theory of magnetic storms and of the aurorae, Kgl. Sv, Vetenskapsakad. Handl., 18, 3, 1939.

Alfven,H., Cosmical electrodynamics, Oxford University Press, London, 1950.

Alfven,H., Magnetic storms and the aurorae: a reprint of selected portions of the 1939 article by H. Alfven, EOS Trans.,AGU 51,180,1970.

Akasofu,S.-I., Dynamical morphology of the aurora polaries, J. Geophys. Res., 68,1667,1963..

Bostrom,R.,A model of the auroral electrojets, J. Geophys. Res., 69,4983,1964.

Burke,W.J., A theoretical investigation of small scale auroral zone electric fields and their relation to particles precipitation patterns,Ph.D thesis, Massachusetts Institute of Technology, Cambridge, Mass.

Cloutier,P.A., Vector measurement of the mid-latitude Sq ionospheric current system, Ph.D. thesis, Rice Univ., Houston, Texas.

Davis,T.N., The morphology of the auroral displays of 1957-1958 ;2. Detailed analyses of Alaska data and analyses of high-latitude data, J. Geophys. Res., 67,75,1962.

Dungey,J.W., Interplanetary magnetic field and the auroral zones, Phys. Rev. Letters, 6, 47, 1961.

Heppner,J.P., A study of relationships between the aurora borealis and the geomagnetic disturbances caused by electric currents in the ionosphere, Ph.D. thesis, California Institute of Technology, Pasadena, 1954.

Hill,J.E., Auroral heights over Churchill, Manitoba, during International Quiet Solar Year, Can. J. Phys., 43, 1917.

Jensen,D.C., and H.C.Cain, An interim geomagnetic field (Abstract), J. Geophys. Res., 67, 3568; corresponding report, Jensen D.C., Dikewood Corp. Albuquerque,N.M., Final Report, Contract NAS 5-1278,1962.

Kim,J.S., and R.A.Volkman, Thickness of zenithal auroral arcs over Fort Churchill, Canadam J. Geophys. Res., 68,3187,1963.

Park,R.J., Rockey-borne magnetometer measurement of field aligned currents associated with an auroral arc, Ph.D. thesis, Rice Univ., Houston, Texas.

Park,R.J., and P.A.Cloutier, Rocket-based measurement of Birkeland currents related to an auroral arc and electrojet, J.Geophys. Res., 76,7714,1971.

Sandel,B.R., Electric currents associated with an auroral arc, Ph.D. thesis, Rice Univ.,Houston, Texas, 1972.

Sesiano,J., Rocket attitude determination using a vector magnetometer, M.S. thesis, Rice Univ. Houston,Texas.

Vondrak,R.R., Rocket-borne measurement of auroral particles currents, Ph.D. thesis, Rice Univ., Houston, Texas, 1970.